Biomaterials 338 (2027) 124691



Contents lists available at ScienceDirect

Biomaterials

journal homepage: www.elsevier.com/locate/biomaterials





Rare-earth-free magnesium-zinc alloy with controlled biodegradation and biocompatibility for novel biodegradable metallic stent

Yubeen Park [a], Yerin Ha [a,b,c], Hyung Jin Roh [d], Hyun Lee [e], Seung Jin Eo [a,c], Do-Yoon Kang [f], Nayoung Lee [g], Hyun-Do Jung [g], Jun-Kyu Park [h], Kang-Sik Lee [a], Yu-Chan Kim [i,j], Hwa-Chul Jung [d], Joung Sik Suh [k], Jung-Hoon Park [a,c,*]

[a] Biomedical Engineering Research Center, Asan Institute for Life Sciences, Asan Medical Center, 88 Olympic-ro 43-gil, Songpa-gu, Seoul, 05505, Republic of Korea
[b] Department of Medical Science Convergence, Graduate School of Medical Science, University of Ulsan, 93, Daehak-ro, Nam-gu, Ulsan, 44610, Republic of Korea
[c] Department of Convergence Medicine, Asan Medical Center, University of Ulsan College of Medicine, 88 Olympic-ro 43-gil, Songpa-gu, Seoul, 05505, Republic of Korea
[d] CG MedTech Co., Ltd., 20 Sandan-ro 76beon-gil, Uijeongbu-si, Gyeonggi-do, 11781, Republic of Korea
[e] Research Institute of Intelligent Manufacturing & Materials Technology, Korea Institute of Industrial Technology, 156, Gaetbeol-ro, Yeonsu-gu, Incheon, 21999, Republic of Korea
[f] Division of Cardiology, Department of Internal Medicine, Asan Medical Center, University of Ulsan College of Medicine, 88 Olympic-ro 43-gil, Songpa-gu, Seoul, 05505, Republic of Korea
[g] Division of Materials Science and Engineering, Hanyang University, 222, Wangsimni-ro, Seongdong-gu, Seoul, 04763, Republic of Korea
[h] IMT Inc., 45 Jami-ro 6beon-gil, Buk-gu, Gwangju, 61226, Republic of Korea
[i] Biomaterials Research Center, Biomedical Research Division, Korea Institute of Science and Technology (KIST), Seoul, 02792, Republic of Korea
[j] Division of Bio-Medical Science and Technology KIST School, Korea University of Science and Technology, Seoul, 02792, Republic of Korea
[k] Lightweight Materials Research Division, Korea Institute of Materials Science, Changwon, 51508, Republic of Korea

ARTICLE INFO

Keywords:
Biodegradable stent
Magnesium alloy
Rare-earth-free
Magnesium-zinc alloy
Biocompatibility
Vascular stent

ABSTRACT

Biodegradable magnesium (Mg) alloy stents offer a transient alternative to permanent metallic implants; however, clinically used WE43 contains rare-earth (RE) elements, raising concerns regarding the long-term biosafety of RE-containing degradation products and their potential tissue accumulation. Here, we investigated two RE-free Mg–Zinc (Zn)-based alloys, MZ01 (Mg–1Zn–0.1Ca) and ZM115 (Mg–1Zn–1.5Mn–0.5Sr), and established a mechanistic cascade linking alloy composition and microstructure to electrochemical analyses revealed alloy-dependent differences in grain structure and interfacial corrosion resistance, with MZ01 exhibiting the highest charge-transfer resistance. In a mouse subcutaneous model, MZ01 showed more uniform degradation, smaller and more rapidly resolving hydrogen gas cavities, and a significantly lower microcrack area fraction at Day 56 than WE43 and ZM115, accompanied by attenuated inflammatory and fibrotic responses. In the rabbit iliac arteries, all stents maintained luminal patency without thrombosis through 56 days, while MZ01 exhibited lower neointimal thickness, lower perivascular apoptosis and late inflammation, and enhanced early endothelialization compared with WE43. Preliminary descriptive porcine coronary implantation further demonstrated the technical feasibility and sustained patency of MZ01 over 56 days. Collectively, these findings define a composition–microstructure–corrosion–cellular response–vascular healing axis and identify MZ01 as a RE-free Mg–Zn alloy with controlled biodegradation and favorable biocompatibility, supporting its further development as a biodegradable cardiovascular scaffold.

1. Introduction

Cardiovascular diseases pose a significant global health challenge, with coronary artery disease being a leading cause of morbidity and mortality [1]. Interventional treatment strategies have evolved from balloon angioplasty to coronary artery stenting to restore and maintain luminal patency [2,3]. Introduced in the 1980s, bare metal stents (BMSs) have successfully overcome the limitations of balloon

* Corresponding author. Department of Convergence Medicine, Asan Medical Center, University of Ulsan College of Medicine, 88 Olympic-ro 43-gil, Songpa-gu, Seoul, 05505, Republic of Korea.
E-mail address: jhparkz@amc.seoul.kr (J.-H. Park).

https://doi.org/10.1016/j.biomaterials.2026.124691
Received 23 July 2026; Received in revised form 6 October 2026; Accepted 10 October 2026
Available online 15 October 2026
0142-9612/© 2026 The Authors. Published by Elsevier Ltd. This is an open access article under the CC BY license (http://creativecommons.org/licenses/by/4.0/).

angioplasty, such as acute vessel recoil and constrictive remodeling [4,5]. However, BMSs, typically fabricated from stainless steel or cobalt-chromium alloys, remain permanently within blood vessels, which can lead to inflammation, thrombosis, and in-stent restenosis (ISR) due to excessive neointimal hyperplasia [6,7]. These shortcomings have prompted the development of biodegradable stents and scaffolds, which provide temporary mechanical support and subsequently degrade and disappear after tissue healing [8–10]. Among them, biodegradable polymer-based stents, such as poly-L-lactic acid, suffer from insufficient toughness and mechanical strength, requiring high molecular weight and thicker stent struts, which in turn leads to longer degradation times and poor vascular compliance [11,12]. Accordingly, biodegradable metallic stents with enhanced mechanical strength and deformability have attracted considerable attention [13].

Magnesium (Mg) is an essential macro-element in the human body, and its corrosion products can be absorbed or excreted through normal metabolism, making it a promising material for cardiovascular stents [14,15]. Mg alloy stents can be degraded and completely absorbed *in vivo*, thus avoiding ISR resulting from neointimal hyperplasia caused by a long-term foreign body reaction [16]. Following these advantages, several Mg alloy stents, such as AMS-1 (Biotronik AG, Bülach, Switzerland) and DREAMS (Biotronik AG), have demonstrated clinical feasibility [17–19]. These stents are based on the WE43 alloy, which remains the only Mg alloy to have received CE mark approval for clinical use [20]. WE43 contains rare earth (RE) elements and exhibits favorable mechanical properties and corrosion resistance [21]. Nevertheless, because RE elements are not naturally present in the human body, their long-term biocompatibility in cardiovascular applications requires further investigation [22,23].

Recently, Mg–Zn series alloys, including MZ01 (Mg–1Zn–0.1Ca) and ZM115 (Mg–1Zn–1.5Mn–0.5Sr), have been proposed as RE-free alternatives for biodegradable materials [24,25]. Instead of incorporating RE elements, these alloys were designed using biologically relevant alloying elements to mitigate concerns regarding long-term biocompatibility

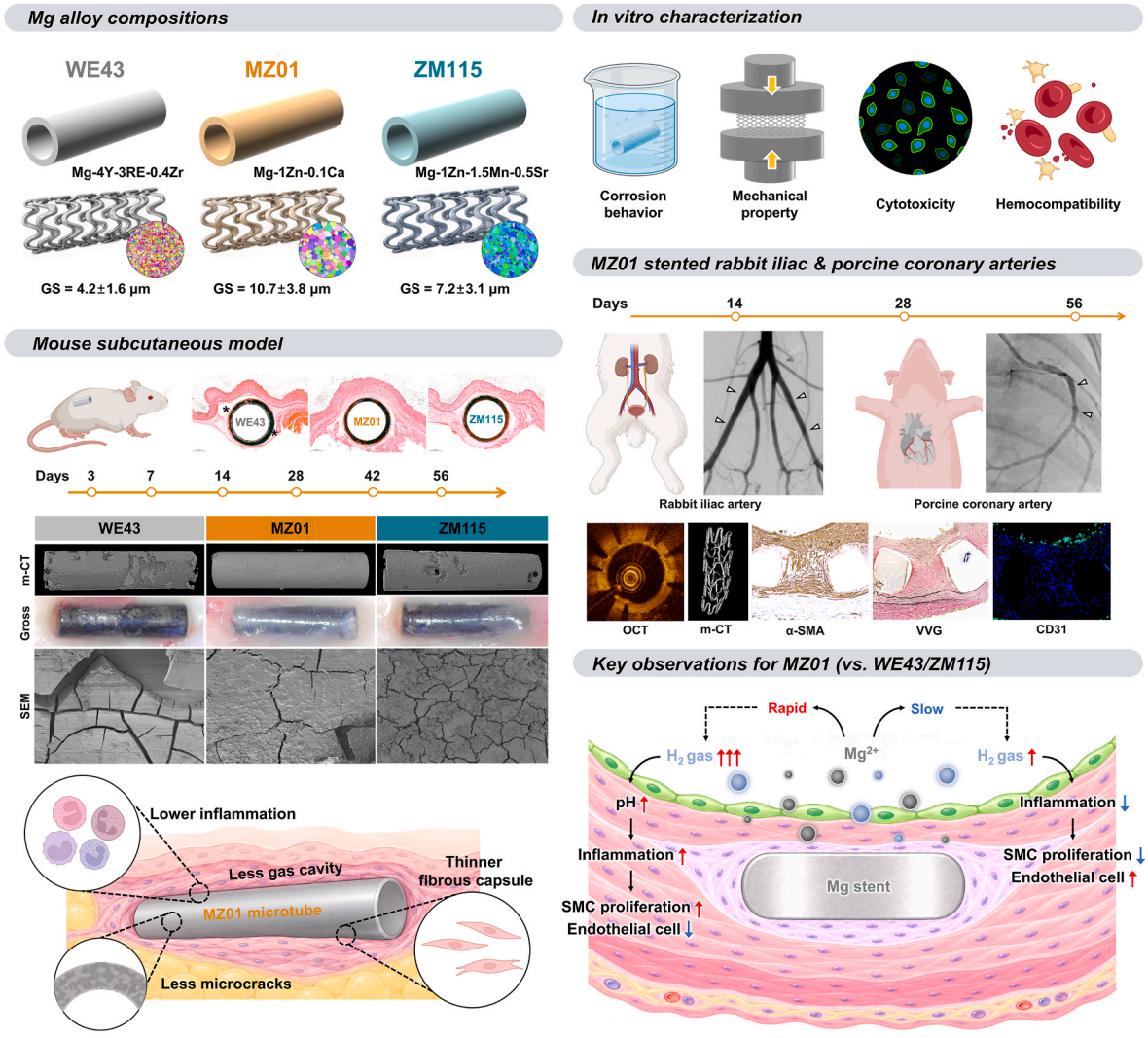

Scheme 1. Schematic overview of the composition–degradation–biological response relationship of WE43, MZ01, and ZM115 biodegradable magnesium (Mg) alloys. The alloy compositions, fabricated microtubes/stents, and corresponding grain sizes (GS) of WE43 (Mg–4Y–3RE–0.4Zr), MZ01 (Mg–1Zn–0.1Ca), and ZM115 (Mg–1Zn–1.5Mn–0.5Sr). *In vitro* characterization included evaluation of corrosion behavior, mechanical properties, cytotoxicity, and hemocompatibility. *In vivo* biodegradation and tissue responses were investigated using a mouse subcutaneous implantation model over 56 days. Compared with WE43 and ZM115, MZ01 exhibited fewer surface microcracks, reduced gas cavity formation, lower inflammatory responses, and a thinner fibrous capsule, indicating more controlled biodegradation and improved local tissue compatibility. Vascular performance of MZ01-based stents was further evaluated in rabbit iliac and porcine coronary arteries. The proposed mechanism linking Mg degradation rate to vascular responses: relatively rapid degradation may increase Mg^{2+} release, local alkalization, and hydrogen (H_2) gas evolution, thereby sustaining inflammation and promoting smooth muscle cell (SMC) proliferation and neointimal formation, whereas more controlled degradation may attenuate inflammation, limit neointimal hyperplasia, and facilitate endothelial recovery.

[26]. MZ01 represents a simplified Mg–Zn–Ca system designed to achieve a favorable balance between mechanical integrity, degradation control, and biocompatibility, whereas ZM115 represents a multicomponent Mg–Zn–Mn–Sr system intended to further modulate microstructural refinement, impurity-related corrosion, and biological responses [27,28]. Although MZ01 has been reported as a promising biodegradable Mg alloy, the *in vivo* vascular performance and safety of Mg–Zn-based alloys, including ZM115, have not been systematically evaluated, particularly in cardiovascular stent applications [25]. Therefore, this study aimed to assess the biocompatibility, biodegradation behavior, technical feasibility, and safety of MZ01 and ZM115 using a mouse subcutaneous model and a rabbit iliac artery stent model, with the clinically used WE43 alloy as a reference control (Scheme 1). Overall, MZ01 exhibited biocompatibility and biodegradation behavior comparable to, and in some respects more favorable than, those of the clinically used RE-containing Mg alloy WE43. Based on these findings, an additional porcine coronary artery stent evaluation was performed using MZ01 to provide preliminary evidence of translational feasibility in a clinically relevant large-animal model. Collectively, these findings suggest that the MZ01 alloy may provide a promising alternative material platform for the development of biodegradable cardiovascular stents.

2. Materials and methods

2.1. Preparation of magnesium alloy and microtubes

Two RE-free Mg–Zn-based alloys, MZ01 (Mg–1Zn–0.1Ca) and ZM115 (Mg–1Zn–1.5Mn–0.5Sr), were used in this study. A commercially available RE-containing alloy, WE43 (Mg–4Y–3RE–0.4Zr; Magnesium Elektron Ltd., Manchester, UK), was used as the reference control. The chemical compositions of all alloys are listed in Table S1. Microtubes were fabricated via a two-step direct extrusion process, as previously reported [25,29]. Briefly, alloy billets were extruded at 400°C into solid rods (15.9 mm in diameter) with an extrusion ratio of 25:1. The first-extruded rods was machined into hollow billets with an outer diameter of 13.9 mm, an inner diameter of 1.8 mm, and a height of 25 mm. The hollow billets were subsequently extruded using a 500-ton horizontal extruder. MZ01 and ZM115 were extruded at 420°C, while WE43 was extruded at 450°C to produce microtubes with a length of approximately 2 m. MZ01 and ZM115 microtubes had an outer diameter of 2.1 mm and a wall thickness of 0.2 mm. WE43 microtubes had an outer diameter of 2.0 mm and a wall thickness of 0.2 mm due to low extrudability (Fig. S1A).

2.2. Microstructural and electrochemical characterization of WE43, MZ01, and ZM115 microtubes

Transverse cross-sections of the as-extruded WE43, MZ01, and ZM115 microtubes were examined by scanning electron microscopy (SEM, JEOL JSM-7800F; JEOL Ltd., Tokyo, Japan) with an electron backscatter diffraction detector (EBSD, Oxford Symmetry; Oxford Instruments, High Wycombe, UK). EBSD maps were acquired at an accelerating voltage of 15 kV with a step size of 0.3 μm over an area of $150 \times 180\ \mu m^2$. Data acquired using AZtec software (ver. 6.2; Oxford Instruments) were analyzed using OIM analysis software (ver. 8.6.; EDAX Inc., Mahwah, NJ, USA). The evaluated microstructural parameters included area-weighted grain size (GS), mean first-neighbor kernel average misorientation (KAM_{1st}), maximum (0001) pole-figure intensity (I_{max}), and mean Schmid factors for basal <a> slip (m_{basal}) under tension loading along the extrusion direction.

Electrochemical measurements were performed using a potentiostat/galvanostat (ZIVE MP1; WonATech Co., Ltd., Seoul, Republic of Korea) and a conventional three-electrode cell containing 1 L of phosphate-buffered saline (PBS; pH 7.4) maintained at 37 ± 1°C. The microtube specimen, a saturated Ag/AgCl electrode, and a graphite rod were used as the working, reference, and counter electrodes, respectively. All measured potentials were converted to the standard hydrogen electrode (SHE), using +0.205 V versus SHE for the saturated Ag/AgCl reference electrode. The working consisted of 30-mm-long microtube segments with both ends sealed in epoxy, leaving the inner and outer surfaces exposed, corresponding to an exposed area of 3.7 cm^2 [29]. The open-circuit potential (OCP) was monitored for 24 h, and electrochemical impedance spectroscopy (EIS) measurements were performed at the OCP after 6, 12, 18, and 24 h using 10 mV perturbation amplitude over a frequency range of 10 kHz–10 mHz. The obtained Nyquist spectra were fitted using ZIVE Data Manager software (ver. 1.60; WonATech Co., Ltd.). Cyclic potentiodynamic polarization (CPP) tests were performed on separate specimens in the same three-electrode configuration in PBS at 37 ± 1°C, in accordance with ASTM F2129−19a. After 2h of OCP stabilization, the potential was scanned from −0.5 V versus OCP to +0.25 V versus OCP, and then reversed to −0.5 V versus OCP at a scan rat of 0.166 mV s^{-1}. The corrosion potential (E_{corr}) and the corrosion current density (I_{corr}) were estimated by Tafel extrapolation.

2.3. Fabrication of WE43, MZ01, and ZM115 stents

Biodegradable WE43, MZ01, and ZM115 stents were fabricated by laser cutting (CG MedTech Co., Ltd., Seoul, Republic of Korea). Extruded metallic tubes (outer diameter, 2.0 mm; inner diameter, 1.8 mm) were used as the starting material for stent fabrication. The stent pattern was cut using a femtosecond laser system (StarCut Tube SL, Coherent) at an average laser power of approximately 3.4 W with nitrogen (N_2) assist gas supplied at 6 bar, with cutting speeds ranging from 2.5 to 5.0 mm/s depending on the cutting region. Optimized cutting parameters were applied separately to general cutting, small-radius, and engraving regions. After laser cutting, the stents were washed twice in 99% ethanol (5 min per cycle) to remove surface oxides, carbonaceous residues, and micro-burrs generated during processing. Electropolishing was performed in a Nital electrolyte (ethanol:nitric acid = 95:5, w/w). Each stent was mounted on a platinum wire and connected as the anode, while a stainless-steel plate served as the cathode. A constant voltage of 10 V was applied using a DC rectifier, generating a current of approximately 0.05 A, corresponding to a current density of approximately 87.4 mA/cm^2 based on the total surface area (57.196 mm^2) calculated from the CAD model. Electropolishing was carried out for 2 min at 25°C under continuous stirring. This process reduced the stent wall thickness from 150 to 130 μm, corresponding to a 13.3% reduction. The electropolished stents (diameter, 2.75 mm; length, 8 mm; strut thickness, 70 μm) were mounted onto custom balloon catheters (nominal diameter, 2.75 mm; length, 12 mm) and crimped to a target diameter of 1.10 mm using a CX crimping system (Blockwise) through a stepwise radial-compression process. No additional annealing or heat treatment was applied at any stage of fabrication (Fig. S1B).

2.4. Surface morphology and elemental characterization of the fabricated stents

The surface morphology and elemental composition of the fabricated WE43, MZ01, and ZM115 stents were examined using field-emission scanning electron microscopy (FE-SEM) equipped with energy-dispersive X-ray spectroscopy (EDS, Sigma 500; Carl Zeiss A.G., Oberkochen, Germany). SEM imaging was used to assess stent surface condition after fabrication, whereas EDS verified the elemental composition of each alloy.

2.5. Characterization of degradation-associated pH changes and Mg ion release

To characterize the degradation behavior of the Mg alloy stents, changes in the pH and Mg ion concentration of the extraction medium were evaluated over time. WE43, MZ01, and ZM115 stents were

immersed in Dulbecco's modified Eagle medium (DMEM) under identical exposure conditions. The samples were incubated at 37°C in a humidified atmosphere containing 5% CO_2 to simulate physiological conditions. Extraction media were collected at 3, 6, 12, 24, 72, and 168 h. The pH of the extraction medium was measured at each time point using a calibrated pH meter. At each designated time point, the extraction medium was collected for Mg^{2+} analysis and replaced with fresh medium. The Mg^{2+} concentration was quantified using the QuantiChrom™ Metal Ion Assay Kit (DIMG-250, BioAssay Systems, USA). The measured Mg^{2+} concentrations were cumulatively summed across all time points and expressed in ppm to characterize the time-dependent Mg^{2+} release profile of each alloy.

2.6. In vitro cytocompatibility of the stent extracts

Mg alloy extracts were prepared from three different alloys (WE43, MZ01, and ZM115) using endothelial basal medium with a surface area-to-extraction medium ratio of 1.25 cm^2/mL, following ISO 10993-5 and ISO 10993-12 guidelines [14]. The extraction was performed 37°C in a humidified atmosphere with 5% CO_2 for 24 h. An extract-based assay was selected, as this approach is commonly used for biodegradable Mg alloys to evaluate the effects of soluble degradation products while minimizing potential interference associated with direct exposure to the biodegradation metal [30]. Human umbilical vein endothelial cells (HUVECs) were used to evaluate *in vitro* biocompatibility. To evaluate cell viability, HUVECs were seeded into 48-well plates at a density of 2×10^4 cells/mL (200 μL/well) and allowed to attach for 24 h. The culture medium was then replaced with alloy extracts diluted to various concentrations (10%, 50%, and 100%). After incubation for 1, 3, and 5 d, cell viability was quantitatively assessed using a D-Plus cell counting kit-8 (CCK-8) solution and incubated for 2 h. The optical density was measured at 450 nm using a microplate reader.

To assess the endothelial cell morphology, HUVECs were seeded into 24-well plates at a density of 1×10^4 cells/mL (500 μL/well) and cultured with the extracts for 1, 3, and 5 d. Following incubation, the cells were fixed with 4% paraformaldehyde for 5 min, permeabilized with 0.5% Triton X-100 (10 min at room temperature (RT)) and blocked with 3% bovine serum albumin (1 h at RT). For cytoskeleton and nuclei visualization, F-actin and cell nuclei were stained with phalloidin (30 min at RT) and 4′,6-diamidino-2-phenylindole (DAPI, 1:1000, 10 min at RT), respectively. The stained cells were observed and photographed using a Nikon Eclipse Ti2-U microscope (Nikon, Tokyo, Japan).

2.7. Mechanical properties of the fabricated WE43, MZ01, and ZM115 stents

The mechanical performance of the fabricated Mg stents (WE43, MZ01, and ZM115) was evaluated in terms of radial force, flexibility, recoil, and foreshortening [31]. All stents had a nominal diameter of 2.75 mm and were expanded using a balloon catheter at 8 atm. Radial force and flexibility were measured using a universal testing machine (EMX-1000 N II; IMADA Co., Ltd., Toyohashi, Japan). The radial force was measured by compressing the expanded stent to 50% of its diameter at a constant speed (15 mm/min), and the corresponding force was recorded (Fig. S2A). Flexibility was assessed using a three-point bending test, where the stent was placed on separate jigs and displaced by half of its nominal diameter at a displacement rate of 15 mm/min (Fig. S2B). Foreshortening was calculated to quantify the longitudinal shortening of the stent after balloon dilation, defined as the difference between the crimped length (L_c) and the expanded length (L_e): Foreshortening (%) = $(L_c - L_e)/L_c \times 100$. Recoil ratio was calculated to quantify the reduction in stent diameter after balloon dilation, defined as the difference between the expanded diameter (D_e) and the diameter after recoil (D_r) after balloon dilation: Recoil (%) = $(D_e - D_r)/D_r \times 100$.

2.8. In vitro hemocompatibility evaluation

Hemocompatibility was performed according to ISO 10993-4. Hemolysis and whole blood coagulation analyses were performed to evaluate the *in vitro* hemocompatibility of the Mg stents. Porcine blood samples were obtained by venipuncture, and 3.8 wt% sodium citrate was added as an anticoagulant. The degree of hemolysis was compared using red blood cells. Three different Mg alloy stents (WE43, MZ01, and ZM115) were placed in tubes containing normal saline (5 mL) and diluted whole blood (0.1 mL). The tubes were incubated in a 37°C water bath for 1 h. A combination of saline solution (5 mL) and whole blood (0.1 mL) served as the negative control, whereas a mixture of distilled water (DW, 5 mL) and whole blood (0.1 mL) was used as the positive control. The samples were subsequently centrifuged for 5 min at 3000 rpm, and the absorbance of the resulting supernatant was measured at 545 nm using a microplate reader (Synergy HTX; BioTek, Winooski, VT, USA). The percentage of hemolysis was calculated to evaluate the hemolytic activity, defined as the ratio of the difference between the sample optical density (OD_t) and the negative control (OD_{nc}) to the difference between the positive control (OD_{pc}) and the negative control (OD_{nc}): Hemolysis (%) = $[(OD_t - OD_{nc})/(OD_{pc} - OD_{nc})] \times 100$. Blood coagulation tests were performed by incubating citrated whole blood with the stent, followed by the addition of a coagulation reagent comprising 0.1 M calcium chloride solution at 37°C for 10 and 30 min. The stents were gently rinsed with DW and then vigorously shaken for 1 min to obtain a homogeneous solution. The whole blood coagulation index was determined to quantify the blood clotting behavior, defined based on the absorbance of anticoagulated whole blood in contact with the stent (A_s) relative to the absorbance of DW (A_w): Blood coagulation index (%) = $(1 - A_s/A_w) \times 100$ [32].

2.9. Animal study design of mouse subcutaneous implantation model

The *in vivo* study was approved by the Institutional Animal Care and Use Committee of Asan Institute for Life Sciences (#2025-40-162) and conformed to the guidelines of the USA National Institutes of Health for handling laboratory animals. Thirty-six male BALB/c mice weighing 18.8–22.9 g (mean, 20.5 g; JABIO, Suwon, Korea) were used in this study. The mice were randomly divided into three groups (n = 12 per group) according to the Mg microtube implanted (WE43, MZ01, and ZM115). All mice underwent subcutaneous implantation of microtubes and were euthanized at 3, 7, 14, 28, 42, and 56 days after implantation (n = 2 per time point for each group).

2.10. Mouse subcutaneous implantation of Mg microtubes

The mice were anesthetized with isoflurane, and the dorsal hair was removed. Approximately two 5 mm skin incisions were made bilaterally on the back, and subcutaneous pockets were created by blunt dissection. Two microtubes of the same alloy were implanted in each mouse: one in the right-side pocket for histological evaluation and the other in the left-side pocket to observe the surface morphology of the extracted microtubes. The incisions were closed with sutures. Radiographic imaging was obtained before euthanasia to monitor the *in vivo* status of the implanted microtubes. All animals were supplied with food and water ad libitum and maintained at a temperature of 24 ± 2°C with a 12-h day–night cycle. All mice were euthanized at the appointed time points by administering inhalable pure carbon dioxide.

2.11. Characterization of extracted microtube samples

Implanted Mg microtubes and the surrounding tissues were surgically extracted at each time point. All extracted microtubes with tissues were photographed and grossly inspected for the presence of gas cavities associated with biodegradation. Adherent surrounding tissues were carefully removed from the microtubes. The surface morphology of the

extracted microtubes was examined using FE-SEM (Auriga; Carl Zeiss, Baden-Württemberg, Germany). Surface degradation was quantified by measuring the microcracked area on the microtube surface using ImageJ (National Institutes of Health, Bethesda, MD, USA). Microcrack regions were segmented using intensity thresholding, and the cracked area fraction was calculated as the ratio of the segmented crack area to the total region of interest (ROI), as the following equation [33]: microcrack area (%) = microcrack area/total ROI area × 100. The same image-processing procedure was applied to all samples and experimental groups.

2.12. Micro-computed tomography (CT) of extracted microtube samples

The extracted microtube and surrounding tissue were examined using *ex vivo* micro-computed tomography (micro-CT) (SkyScan 1172; Bruker, Billerica, MA, USA). Micro-CT images were acquired at a source voltage of 90 kV and a source current of 88 μA, with an image pixel size of 7.997941 μm, an exposure time of 500 ms, and a rotation step of 0.3°. Four-frame averaging, flat-field correction, random movement, and a 1-mm aluminum filter were applied during image acquisition. The obtained micro-CT scan images were reconstructed using the NRecon software (ver. 1.6.10.4; Bruker) to evaluate the overall microtube morphology. The microtube volume was quantified using the 3D Slicer (Slicer) software (ver. 5.6.2; http://www.slicer.org/) to evaluate the extent of biodegradation. The volume of the non-implanted microtube was defined as the initial volume (100%), and the remaining volume of each extracted microtube was expressed as a percentage of this initial volume. Mg volume loss was calculated as 100 − remaining microtube volume (%).

2.13. Histological examination of the extracted microtube and surrounding tissues

Extracted tissue specimens were fixed in 10% neutral buffered formalin for 48 h, embedded in resin, and sectioned transversely. The sections were stained with hematoxylin and eosin (H&E) and picrosirius red (PSR). H&E-stained sections were evaluated for the degree of inflammatory cell infiltration and the thickness of the fibrous capsule. PSR-stained sections were used to evaluate the degree of collagen deposition. The degrees of inflammatory cell infiltration and collagen deposition were subjectively determined according to the distribution and density of the cells, respectively, using a five-point scale: grade 1 (mild), grade 2 (mild to moderate) grade 3 (moderate), grade 4 (moderate to severe), and grade 5 (severe) [34]. The degree of inflammatory cell infiltration, thickness of fibrous capsule, and degree of collagen deposition were calculated as the average obtained at eight points around the circumference. Histological images were visualized and measured using the CaseViewer software (ver. 2.4.0.119028; 3D HISTECH Ltd., Budapest, Hungary). The histological images were examined by three observers blinded to the study, and a consensus was reached regarding the final report.

2.14. Animal study design of rabbit iliac artery stent model

This study was approved by the Institutional Animal Care and Use Committee of the Asan Institute for Life Sciences (#2025-20-246) and conformed to the United States National Institutes of Health guidelines for humane handling of laboratory animals. This study was also conducted following the ARRIVE guidelines. Thirty-six iliac arteries from 18 New Zealand White rabbits (3.19–4.15 kg; mean, 3.60 ± 0.60 kg; JABIO) were enrolled for analysis. Animals were randomly divided into three groups of six rabbits each according to the placement of the Mg alloy stent (WE43, MZ01, and ZM115). Each rabbit underwent the insertion of two biodegradable stents of the same alloy into both iliac arteries. The enrolled rabbits were euthanized at 14, 28, and 56 days after stent placement (n = 2 rabbits per group at each time point) by intravenous potassium chloride injection.

2.15. Stent placement into the rabbit iliac artery

All rabbits received oral aspirin (10 mg/kg/day) starting 1 week prior to stent placement and continuing until euthanasia [35]. Anesthesia was induced by intramuscular injection of a mixture of zolazepam and tiletamine (Zoletil, 50 mg/kg; Virbac, Nice, France) and xylazine (Rompun, 5 mg/kg; Bayer HealthCare, Leverkusen, Germany) and maintained with 2% isoflurane (Ifran®; Hana Pharm. Co., Seoul, Korea) delivered in a 1:1 oxygen/air mixture (510 mL/kg/min). The left common carotid artery was punctured using an 18-G angiocath (BD Angiocath™ IV Catheter; Becton, Dickinson and Company, Franklin Lakes, NJ, USA), which was then exchanged for a 6-Fr introducer sheath (Terumo, Tokyo, Japan). Heparin (100 units/kg; JW Pharm Co., Seoul, Korea) was administered through the sheath. A 6-Fr guiding catheter (Envoy MPD; Cordis, Hialeah, FL, USA) over a 0.035-inch guidewire (Terumo) was advanced into the abdominal aorta, and pre-procedural angiography was performed to confirm the target vessel diameter and location. Subsequently, the 0.035-inch guidewire was exchanged for a 0.014-inch micro guidewire (Traxcess™ 14; Terumo), which was advanced into the left or right iliac artery. After advancing the balloon catheter with the compressed stent over the guidewire, the balloon was inflated at 6–8 atm for 30 s to achieve a vessel-to-balloon ratio of 1.0:1.1, thereby deploying the stent. Post-procedural angiography was performed to confirm the patency and appropriate positioning. Antibiotics (gentamicin, 80 mg per 2 mL; Shin Poong Pharm Ltd., Seoul, Korea) and analgesics (Keromin, ketorolac 30 mg; Hana Pharm Ltd., Seoul, Korea) were routinely administered for 3 days after the procedure.

2.16. Follow-up angiography

Follow-up angiography was performed immediately after stent placement and at 14, 28, and 56 days after stent placement to check stent patency and any stent-related adverse events. The luminal diameter of the stented iliac artery was measured using Radiant software (version 2023.1; Medixant, Poznań, Poland). Values were normalized to the pre-procedural luminal diameter obtained from baseline angiography and expressed as a percentage to minimize inter-individual anatomical differences using the following formula: luminal patency (%) = (follow-up luminal diameter/pre-procedural luminal diameter) × 100.

2.17. Optical coherence tomography (OCT)

Optical coherence tomography (OCT, Aurios™; Dotter Inc., Incheon, Korea) examination was performed at the same time points as the angiography follow-up using an OCT imaging catheter (Benetis™; Dotter Inc.). After calibration, the OCT catheter was advanced distal to the stented segment over a 0.014-inch guidewire. The acquired OCT images were analyzed to quantify neointimal thickness and the percentage of the stenotic area. Neointimal thickness was defined as the radial distance from the luminal boundary to the inner surface of the neointima, and the percentage of stenotic area was calculated as follows: stenotic area (%) = (1 – luminal area/stent area) × 100.

2.18. Ex vivo micro-CT of extracted stented rabbit iliac artery

The extracted stented iliac artery was examined using *ex vivo* micro-CT at 14, 28, and 56 days after stent placement. The obtained micro-CT scan images were reconstructed, and each stent volume was quantified to evaluate the extent of biodegradation *in vivo*. Changes in stent morphology over time were visualized through three-dimensional rendering and representative cross-sectional views.

2.19. Histological examinations

Tissues fixed in 10% neutral-buffered formalin for 48 h were embedded in paraffin and sectioned transversely into 3-μm-thick slices. The slides were stained with H&E and Verhoeff-Van Gieson (VVG). H&E staining was performed to evaluate the degree of inflammatory cell infiltration and neointimal thickness. The degree of inflammatory cell infiltration was graded from 1 (mild) to 5 (severe) depending on the density and distribution of inflammatory cells around the struts [36]. The degree of arterial injury was quantified via VVG staining and defined as follows: 1, circumscribed rupture of the internal elastic lamina (IEL), without involvement of the media; 2, laceration or rupture of the media involving the IEL; 3, laceration or rupture of the adventitia involving the IEL and media [37].

2.20. Immunohistochemical examination

Immunohistochemistry (IHC) was performed on sliced paraffin-embedded tissues using antibodies against alpha-smooth muscle actin (α-SMA), terminal deoxynucleotidyl transferase-mediated dUTP nick-end labeling (TUNEL), and CD31. The α-SMA- and TUNEL- -positive depositions were scored subjectively using the following criteria: grade 1, mild; grade 2, mild to moderate; grade 3, moderate; grade 4, moderate to severe; and grade 5, severe. For the endothelialization assessment, the CD31-positive area was quantified by measuring the percentage of the positive-stained region within the ROI. The histological and IHC images were examined by three observers blinded to the study, and a consensus was reached regarding the final report.

2.21. Preliminary animal study design of porcine coronary artery model

This study was approved by the Institutional Animal Care and Use Committee of the Asan Institute for Life Sciences (#2026-20-188) and conformed to the United States National Institutes of Health guidelines for humane handling of laboratory animals. To provide preliminary evidence of translational feasibility in a clinically relevant large-animal model, only MZ01 stents, which proved to be most suitable in previous mouse and rabbit *in vivo* studies, were implanted into the coronary arteries. The animal study was approved by the Institutional Animal Care and Use Committee of Asan Institute for Life Sciences and conformed to the guidelines of the USA National Institutes of Health for handling laboratory animals. Three minipigs weighting 28.05–31.35 kg (mean, 30.07 kg; APURES Co., Ltd., Pyeongtaek, Republic of Korea) were used in this study. Each animal received two stents: one in the right coronary artery (RCA) and the other in either the left anterior descending artery (LAD) or the left circumflex artery (LCx), chosen based on the reference vessel diameter. One animal was euthanized at each of the following time points: Days 14, 28, and 56 after stent placement ($n = 1$ per time point). All pigs were administered 100 mg of aspirin and 75 mg of clopidogrel two days prior to stent implantation and continued daily until euthanasia. Vascular access was achieved via the carotid artery using a 6-Fr introducer sheath, and heparin (100 U/kg) was administered. Nitroglycerin was used for vasodilation, and a stent was inserted to achieve a stent-to-vessel ratio of approximately 1.1:1.0. Follow-up angiography and OCT were performed immediately after stent placement and before euthanasia to measure luminal diameter, neointimal thickness, and stenotic area. Upon euthanasia, the stented coronary arteries were extracted, fixed, and processed for H&E staining. The degree of inflammatory cell infiltration was assessed on a grade from 1 (mild) to 5 (severe). As the porcine evaluation was conducted as a pilot study with a limited sample size, all corresponding quantitative observations and schematic representations are presented as preliminary descriptive data and should not be interpreted as definitive statistical evidence.

2.22. Statistical analysis

Data are expressed as mean ± standard deviation. Differences between groups were analyzed using a two-way analysis of variance (ANOVA). Tukey's test was used as the post-hoc test for the ANOVA. Statistical analyses were performed using SPSS software (version 28; IBM, Chicago, IL, USA), and $p < 0.05$ was considered statistically significant.

3. Results and discussion

3.1. Microstructure-dependent electrochemical behavior of WE43, MZ01, and ZM115 microtubes

The EBSD results from transverse cross-sections of the as-extruded WE43, MZ01, and ZM115 microtubes are presented in Fig. 1A. All alloys exhibited predominantly equiaxed grains, and their KAM_{1st} values were nearly identical (0.53–0.54°), with more than 97% of the mapped points showing KAM values below 1°. This indicates that all microtubes were almost fully recrystallized after the second extrusion step and retained comparably low intragranular misorientation. In contrast, GS differed markedly among the alloys: WE43 had the finest grains (4.2 ± 1.6 μm), followed by ZM115 (7.2 ± 3.1 μm) and MZ01 (10.7 ± 3.8 μm). The alloys also developed different textures. ZM115 showed a typical extrusion fiber texture, in which the (0001) poles were distributed along the periphery of the pole figure; that is, the c-axes were oriented nearly perpendicular to the extrusion direction ($I_{max} = 7.1$ m.r.d.). By contrast, the (0001) poles of WE43 and MZ01 were concentrated at intermediate positions along the A2 direction, with I_{max} values of 8.3 and 11.1 m.r.d., respectively. Related texture modifications have been reported in extruded Mg alloys containing RE elements or Ca [38,39]. Consistent with these textures, the mean Schmid factor for basal <a> slip under tension along the extrusion direction was high for WE43 (0.39) and MZ01 (0.34) but low for ZM115 (0.11), indicating more favorable basal-slip orientations in WE43 and MZ01. Despite its finer grains and qualitatively similar tilted texture, WE43 exhibited a larger surface crack fraction than MZ01 after implantation. Thus, these EBSD descriptors alone cannot fully explain the observed surface damage. Contributions from secondary-phase characteristics, matrix chemistry, and surface-film evolution should also be considered, although their relative contributions require further direct verification.

The EIS spectra revealed time-dependent differences in the interfacial responses of WE43, MZ01, and ZM115 during 6–24 h of immersion in PBS (Fig. 1B–E and Table S2). All alloys exhibited depressed capacitive arcs with low-frequency inductive responses. MZ01 consistently showed the highest fitted R_{ct}, decreasing from 1035 Ω cm^2 at 6 h to 755 Ω cm^2 at 18 h before increasing to 834.7 Ω cm^2 at 24 h. In comparison, R_{ct} decreased continuously from 772.4 to 337.9 Ω cm^2 for WE43 and from 708.5 to 542.2 Ω cm^2 for ZM115. Consequently, the fitted R_{ct} ranking was MZ01 > WE43 > ZM115 at 6 h but MZ01 > ZM115 > WE43 from 12 h onward. At 24 h, MZ01 exhibited R_{ct} values approximately 2.47 and 1.54 times those of WE43 and ZM115, respectively. These results suggest that MZ01 maintained greater resistance to interfacial charge transfer under the tested conditions. Its late increase in R_{ct} may reflect changes in surface-film coverage or interfacial reaction kinetics, although the spectra alone cannot distinguish between these possibilities. The CPE exponent decreased from 0.852 to 0.770 for WE43, 0.664 to 0.573 for MZ01, and 0.702 to 0.534 for ZM115, indicating increasingly nonideal capacitive responses. However, the exceptionally large fitted R_L values for MZ01 (10^9–10^{11} Ω cm^2) require parameter-identifiability checks before being used for mechanistic interpretation. The EIS results therefore support differences in interfacial behavior without independently establishing the corresponding *in vivo* degradation rates.

The CPP responses are summarized in Fig. 1F–H and Table S3. The apparent corrosion potentials shifted negatively from −1.35 to −1.44 V

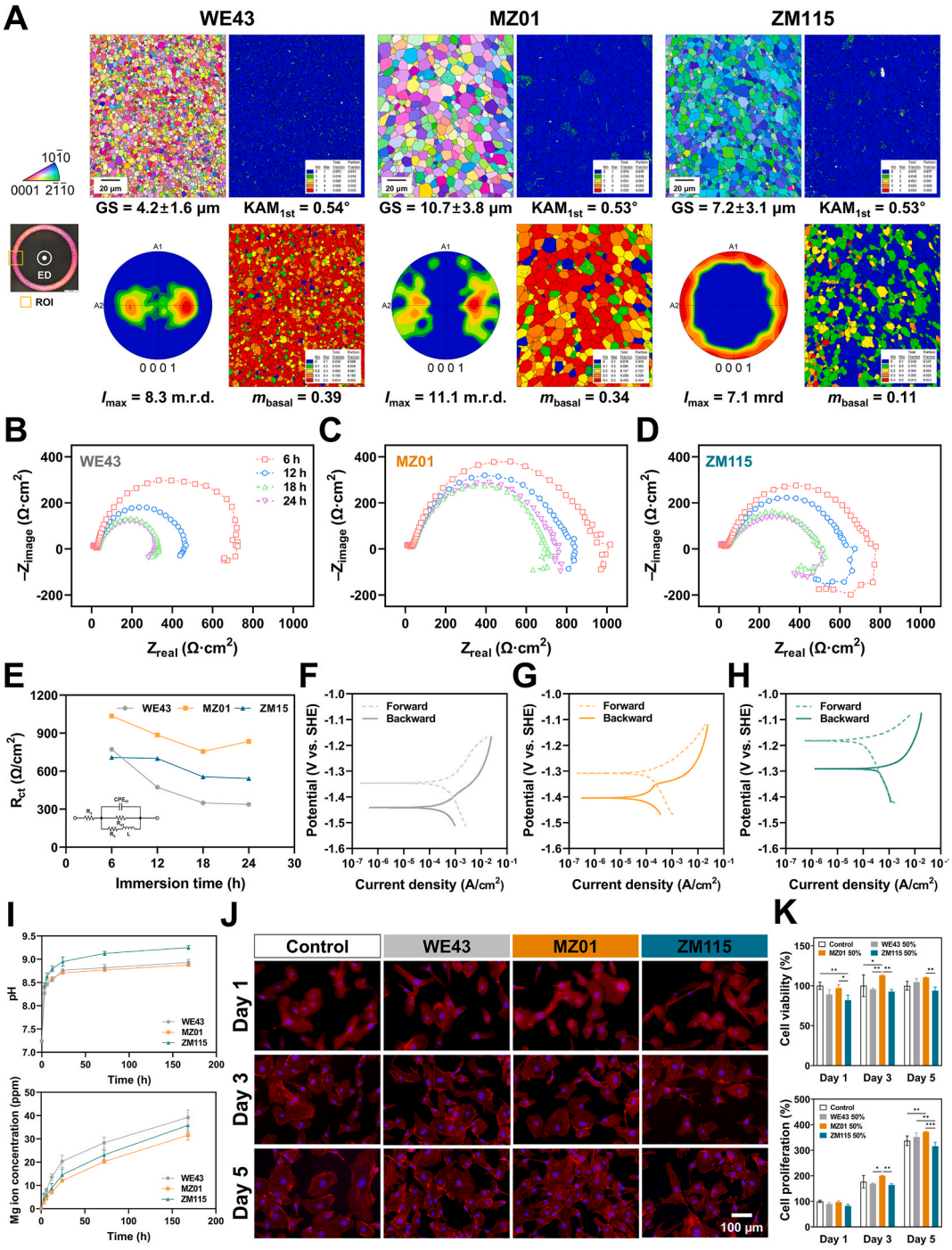

Fig. 1. Microstructural, electrochemical, degradation, and cytocompatibility characteristics of WE43, MZ01, and ZM115 Mg alloys. (A) Electron backscatter diffraction (EBSD) analysis of transverse cross-sections of the as-extruded microtubes, showing inverse pole figure orientation map, first-neighbor kernel average misorientation map, (0001) pole figure, and Schmid factor map for basal <a> slip under tensile loading along the extrusion direction. Nyquist plots obtained by electrochemical impedance spectroscopy (EIS) after 6, 12, 18, and 24 h of immersion for (B) WE43, (C) MZ01, and (D) ZM115. (E) Changes in fitted charge-transfer resistance (R_{ct}). The inset shows the equivalent circuit used for fitting the EIS spectra. Cyclic potentiodynamic polarization curves of (F) WE43, (G) MZ01, and (H) ZM115, showing forward and reverse polarization scans. (I) Time-dependent changes in pH and Mg-ion concentration during immersion, reflecting degradation-associated alkalization and Mg release from the three alloys. (J) Representative fluorescence microscopy images reveal the cellular morphology, nuclei (DAPI, blue) and cytoskeleton (Phalloidin, red) of human umbilical vein endothelial cells (HUVECs) cultured for 1, 3, 5 days with each stent extracted diluted to 50%. (K) Quantitative analysis of cell viability and proliferation in the 50% diluted extract were expressed as the ratio of viable cells to the control group. Data are presented as mean ± standard deviation. IPF, inverse pole figure; KAM, kernel average misorientation; ROI, region of interest. $^{*}p < 0.05$, $^{**}p < 0.01$, and $^{***}p < 0.001$. (For interpretation of the references to color in this figure legend, the reader is referred to the Web version of this article.)

for WE43, −1.31 to −1.40 V for MZ01, and −1.18 to −1.29 V versus SHE for ZM115. Although ZM115 maintained the most positive potential, this did not consistently correspond to the lowest estimated corrosion current density. During the forward scan, i_{corr} decreased in the order WE43 (4.96×10^{-4} A cm^{-2}) > MZ01 (1.55×10^{-4} A cm^{-2}) > ZM115 (1.31×10^{-4} A cm^{-2}). During the backward scan, MZ01 exhibited the lowest i_{corr} (1.74×10^{-4} A cm^{-2}), followed by ZM115 (3.98×10^{-4} A cm^{-2}) and WE43 (4.82×10^{-4} A cm^{-2}). The estimated i_{corr} of ZM115 increased approximately threefold between scans, whereas MZ01 showed a smaller increase of approximately 12% and WE43 changed little. This contrast suggests a greater dependence of the ZM115 polarization response on prior electrochemical exposure. Changes in surface-film coverage or reaction kinetics could contribute, but the curves alone cannot identify the underlying mechanism. The comparatively low backward-scan i_{corr} of MZ01 is qualitatively consistent with its higher fitted R_{ct} in the EIS measurements. Nevertheless, the forward-scan ranking differs, highlighting the influence of measurement history. Because Tafel-derived values for Mg alloys can differ from independently measured corrosion rates, these results should be interpreted as protocol-dependent electrochemical responses rather than direct predictions of *in vivo* degradation.

3.2. Surface characterization of fabricated WE43, MZ01, and ZM115 stents

WE43, MZ01, and ZM115 alloy stents were successfully fabricated by laser cutting using the same protocol. Each stent adhered to the specified dimensions, with a nominal diameter of 2.75 mm, a length of 8 mm, and a strut thickness of 70 μm. Visual inspection revealed consistent and well-defined strut patterns across all alloy types, with no observable defects such as strut fractures, incomplete cuts, or significant deformations (Fig. S1B). However, SEM analysis indicated differences in surface morphology among the stents, despite uniform post-processing conditions (Figs. S3 and S4). The MZ01 stents displayed relatively smooth strut surfaces with rounded edges, whereas the ZM115 stents exhibited irregular surface features with noticeable micro-asperities. The WE43 stents exhibited an intermediate surface. Although quantitative surface roughness measurements were not conducted, these qualitative differences suggest that the alloy composition may influence the response to electropolishing [40,41]. Further research is necessary to assess the potential effects of these surface variations on *in vitro* and *in vivo* biological responses of cells. EDS elemental mapping confirmed the compositional identity of each alloy, which closely aligned with the intended nominal compositions (Table S1, Fig. S4, and Fig. S5). Specifically, WE43 stents contained yttrium (Y), RE elements, and zirconium (Zr), while MZ01 (Mg–Zn–Ca) and ZM115 (Mg–Zn–Mn–Sr) stents were nearly devoid of RE elements. Although EDS provides useful information on elemental distribution and allows semi-quantitative assessment of elemental composition, it has inherent limitations in accurately determining bulk elemental composition because the analysis is surface-sensitive and may be affected by factors such as matrix effects and sampling depth. Therefore, the EDS results were used primarily to confirm the presence and distribution of the expected alloying elements rather than for definitive quantitative determination of bulk compositions.

3.3. Alloy-dependent pH evolution and Mg ion release during degradation

The degradation environment of WE43, MZ01, and ZM115 stents was further characterized by measuring changes in pH and Mg ion concentration over time (Fig. 1I). The pH of the extraction medium increased rapidly within the initial 24 h and then increased more gradually up to 168 h, with clear alloy-dependent differences where ZM115 showed the highest pH values (9.25 ± 0.04 at 168 h) while MZ01 (8.88 ± 0.03) and WE43 (8.93 ± 0.07) exhibited lower and comparable levels. Similarly, Mg ion concentrations increased progressively during the extraction period, indicating time-dependent magnesium ion release, with WE43 showing the highest concentration (39.24 ± 3.22 ppm at 168 h) followed by ZM115 (35.81 ± 2.93 ppm) and MZ01 (31.57 ± 2.12 ppm). These results provide quantitative evidence of time-dependent changes in the degradation environment and support the interpretation that the transient cellular responses observed at early time points may be associated with alloy-dependent differences in soluble degradation products and local alkalization. However, because Zn^{2+} and other alloying elements were not quantitatively measured, the specific contribution of individual alloying ions to the observed cellular responses cannot be determined from the present data.

3.4. In vitro cytocompatibility of the stent extracts

The cell viability and proliferation of HUVECs cultured with alloy extracts at 10, 50, and 100% dilutions over 1, 3, and 5 days are presented in Fig. 1J and K and Fig. S6–S8. On Day 1, cell viability decreased overall compared to that in the control group across all alloy groups and dilution concentrations, exhibiting a concentration-dependent pattern. This initial decline was transient, with viability recovering by Days 3 and 5, except for the 100% concentration and ZM115 groups, reaching levels similar to or higher than those of the control group (Table S4 and Fig. S7). Cell proliferation rates also gradually increased over time, but similar to viability, the 100% dilution and ZM115 group showed lower proliferation rates than the control group (Table S5 and Fig. S8). In particular, on Day 5, the proliferation rates of the WE43 and MZ01 groups surpassed those of the control group, and this trend was particularly pronounced at low extract concentrations. This suggests that the degradation products of these alloys may exhibit a weak cell proliferation effect on HUVECs at levels below cytotoxicity. Fluorescence microscopy revealed well-spread cytoskeletal morphology with intact F-actin organization and normal nuclear morphology in HUVECs across all alloy groups and time points, further supporting the cytocompatibility of all three alloys (Fig. 1J and Fig. S6). The transient reduction in cell viability observed on Day 1 across all groups is consistent with the known initial burst release of Mg^{2+} and alloying element ions upon first contact with aqueous media, which can transiently elevate local ion concentrations and osmolality beyond physiological ranges [27]. This early ionic surge is a well-recognized phenomenon in Mg alloy extract studies and typically subsides as ion concentrations equilibrate within the culture medium. The subsequent recovery and above-control viability and proliferation observed at Days 3 and 5 in the WE43 and MZ01 groups suggest that sustained low-level ion release may positively modulate endothelial cell function rather than impair it. Zn^{2+} promotes endothelial cell proliferation and migration at sub-cytotoxic concentrations [42], which may partly account for the enhanced proliferative response observed in MZ01 at later time points. Although all results for ZM115 and the 100% extract showed lower cell viability and proliferation rates compared to the control group at all time points, all three alloys generally maintained cell viability above the 70% threshold relative to the control, which is commonly used as the criterion for cytotoxicity according to ISO 10993-5 [43]. Thus, the present results indicate an absence of overt cytotoxicity under the tested 10%, 50%, and 100% extract conditions. However, these findings should not be interpreted as evidence that the alloys would necessarily be non-adverse to endothelial cells *in vivo*, because extract-based testing does not reproduce the direct interaction between endothelial cells and the stent surface or the complex local environment during stent implantation and degradation. Further direct-contact and *in vivo* studies are therefore warranted to evaluate endothelial responses to the stent surface during endothelialization and progressive biodegradation.

3.5. Mechanical properties of the fabricated WE43, MZ01, and ZM115 stents

The mechanical properties of the fabricated WE43, MZ01, and

ZM115 stents, including radial force, flexibility, foreshortening, and recoil, are presented in Figure S9 and Figure S10. Radial force measurement demonstrated that WE43 exhibited the greatest maximum radial load (2.53 ± 0.29 N), which was significantly greater than that of MZ01 (1.43 ± 0.06 N, $p < 0.001$) and ZM115 (1.33 ± 0.06 N, $p < 0.001$), while no significant difference was observed between MZ01 and ZM115 ($p = 0.768$) (Figs. S9A, B and Fig. S10A). Three-point bending testing revealed that WE43 (0.77 ± 0.06 N) showed a significantly higher maximum bending load compared to MZ01 (0.37 ± 0.06 N, $p < 0.01$) and ZM115 (0.37 ± 0.15 N, $p < 0.01$), with no significant difference between the two RE-free alloys ($p = 1.000$) (Figs. S9C, D and Fig. S10B), suggesting that WE43 was mechanically stiffer and less flexible under this study. Foreshortening was lowest in the ZM115 ($1.76 \pm 0.01\%$), followed by the MZ01 ($3.36 \pm 0.02\%$, $p = 0.138$) and WE43 ($4.15 \pm 0.02\%$, $p < 0.05$) (Fig. S9E and F). Recoil was highest in ZM115 ($7.60 \pm 0.02\%$), with WE43 ($5.52 \pm 0.01\%$, $p < 0.05$) and MZ01 ($4.84 \pm 0.02\%$, $p < 0.01$) showing progressively lower values (Fig. S9E and G). MZ01 exhibited relatively low foreshortening and the lowest recoil among the three alloys, indicating a favorable balance between longitudinal stability and elastic recovery. The mechanical properties of each alloy reflect its composition and influence vascular stent performance [44]. The higher radial force of WE43 may be related to its RE- and Zr-containing composition, which refines grain structure and stabilizes the Mg matrix [45]. Although higher radial force may help maintain luminal patency, excessive force can increase arterial wall stress, vessel injury, and neointimal hyperplasia [46]. Thus, the lower radial force observed in MZ01 and ZM115 may indicate a different mechanical balance relative to WE43, but its clinical relevance should be considered in the context of loading conditions, scaffold design, and deployment site [47]. Regarding flexibility, the lower bending resistance of MZ01 and ZM115 compared to that of WE43 may be associated with improved conformability, which could be beneficial in tortuous vascular segments such as the coronary artery. Foreshortening and recoil are deployment-related metrics. Lower foreshortening may facilitate more accurate stent positioning during deployment, whereas lower recoil may help preserve the expanded lumen after balloon deflation [48]. In this study, MZ01 showed relatively low foreshortening and the lowest recoil, suggesting a comparatively favorable deployment stability under the tested conditions. In contrast, ZM115 exhibited the lowest foreshortening but the highest recoil, indicating reduced length change but less favorable elastic maintenance after expansion. Therefore, within the scope of this study, MZ01 appears to exhibit a more balanced mechanical profile with respect to deployment-related behavior.

3.6. *In vitro hemocompatibility evaluation*

The hemocompatibility of the fabricated stents was evaluated by hemolysis and whole blood coagulation index, and the results are presented in Fig. S9. The calculated blood coagulation index showed no significant variations among the three alloy groups (Fig. S9H), with all specimens preserving stable anti-coagulant profiles relative to one another. The hemolysis rates were $3.03 \pm 1.68\%$ for WE43, $2.50 \pm 1.54\%$ for MZ01, and $2.97 \pm 2.61\%$ for ZM115, which successfully met the international standard safety criteria for biomaterials (less than 5% according to ASTM F756) (Fig. S9I and J). Neither the RE-containing alloy nor the newly developed RE-free alloys impaired red blood cell membrane integrity. These findings indicate that replacing RE elements in MZ01 and ZM115 with physiological alloying elements such as Zn, calcium (Ca), manganese (Mn), and strontium (Sr) does not induce blood coagulation-promoting reactions or local hemolytic cascade reactions.

3.7. *Procedural outcomes and gross findings in a mouse subcutaneous model*

Subcutaneous implantation of Mg microtubes was successfully performed in all mice without procedure-related adverse events or complications. All animals exhibited stable weight gain during the study period, with no significant differences between the groups (Fig. S11). No overt wound complications, such as dehiscence or severe infection, were observed during follow-up. Radiographic evaluations revealed a clear overall contour for all alloys, with WE43 exhibiting a distinct contour (Fig. S12). All microtubes with surrounding tissues were extracted at the designated time points. Gross examination revealed characteristic biodegradation-associated changes, including surface roughening, localized discoloration and the presence of gas cavities within the surrounding tissue. Gas cavity formation is a well-recognized phenomenon during Mg corrosion due to hydrogen evolution and may reflect periods of accelerated corrosion or insufficient local diffusion of generated gas [49]. A gas cavity was initially observed in all alloys at Day 7 (Fig. 2A). However, the significant gas cavities were not observed after Day 14, without any clinical signs of severe inflammation in all groups. The area and degrees of gas cavity formation in the MZ01 group were less than those in the WE43 and ZM115 groups. The extent and frequency of grossly visible gas cavities increased from Day 3 to Day 14 in the WE43 and ZM115 groups and differed across alloys, implying that the balance between corrosion rate and tissue clearance capacity may vary depending on alloy chemistry and corrosion products.

3.8. *Biodegradation behavior with microcrack analysis by FE-SEM*

Biodegradation behavior and progressive surface deterioration of extracted microtubes in all groups were observed as cracks using FE-SEM imaging and are shown in Fig. 2A and summarized in Table S6. Microcracks were observed from Day 3 after implantation in all groups. Early time points were characterized by the appearance of fine surface microcracks and scattered corrosion features. With increasing implantation duration, the microtube surfaces exhibited more pronounced cracking and corrosion-induced roughening. SEM images in the WE43 and ZM115 groups revealed irregular, more localized, and deep corrosion from Day 14 onward compared with the MZ01 group. Quantitative microcrack area analysis confirmed a significant time-dependent increase in the cracked area in all groups, indicating cumulative surface degradation (Fig. 2B and Fig. S13). WE43 microtubes exhibited the highest microcrack area fraction. The mean percentage of microcrack area at Day 56 was lowest in the MZ01 group ($19.61 \pm 5.00\%$), showing a significant difference compared to that in the WE43 ($32.40 \pm 4.10\%$, $p < 0.001$) and ZM115 ($29.82 \pm 6.14\%$, $p < 0.01$) groups, while no significant difference was observed between the WE43 and ZM115 groups ($p = 0.643$) (Fig. 2C). The differences in surface degradation may be associated with the distinct chemistry compositions and microstructural characteristics of the three alloys. Differences in grain size and crystallographic texture may have contributed to the alloy-dependent degradation patterns; however, the finest-grained WE43 exhibited the highest microcrack fraction, suggesting that grain size alone was insufficient to explain the observed *in vivo* degradation. Secondary phase characteristics may also influence localized corrosion through potential micro-galvanic interactions [50,51], although further investigation is required to establish a direct causal relationship between specific secondary phases and the observed degradation patterns. The *in vitro* electrochemical results further support the presence of alloy-dependent interfacial behavior. MZ01 exhibited the highest charge-transfer resistance together with a comparatively low corrosion current density, consistent with its lower microcrack fraction after implantation, whereas WE43 showed lower R_{ct} and the highest microcrack fraction. Taken together, these findings suggest that the observed biodegradation behavior likely reflects the combined effects of alloy chemistry, microstructure, and interfacial electrochemical behavior. Although advanced thermal or thermomechanical treatments can partially mitigate micro-galvanic corrosion by dissolving secondary phases in conventional alloys like WE43 [52], the primary rationale of developing RE-free alloys such as MZ01 lies in inherently avoiding the potential

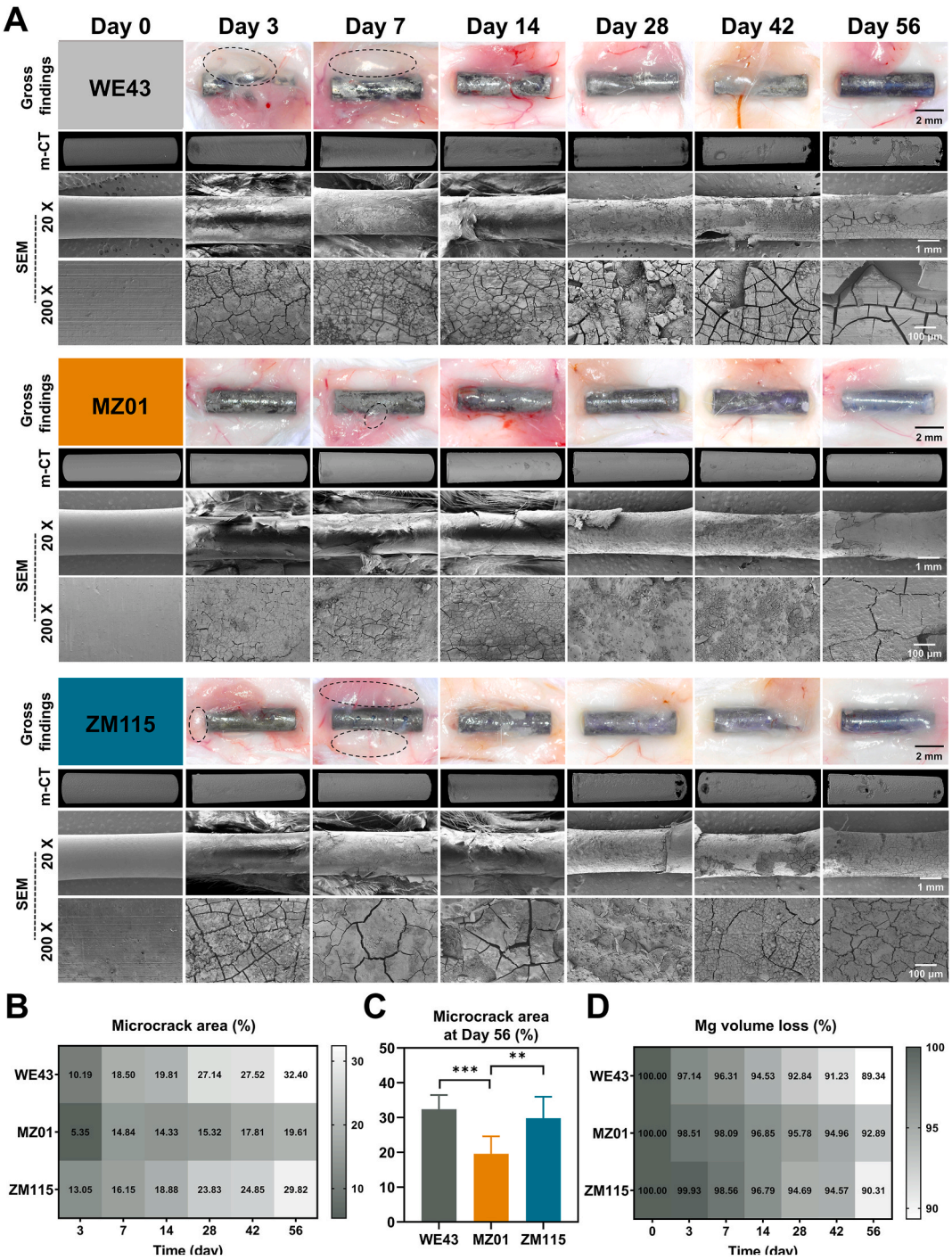

Fig. 2. *In vivo* biodegradation behavior and surface morphological analysis of Mg microtubes (WE43, MZ01, and ZM115) after subcutaneous implantation in mice. (A) Representative images of the extracted Mg microtubes over 56 days. Gross examinations of the microtubes and surrounding tissues were indicated the presence of hydrogen gas cavities (*dotted circles*) during the early stages of biodegradation. The reconstructed three-dimensional image obtained through micro-computed tomography (micro-CT) shows the overall structural integrity and volume changes of the microtubes SEM images at 20× (scale bar = 1 mm) and 200× (scale bar = 100 μm) magnification show the progression of decomposition products and the formation of microcracks on the surface of the microtube. (B) Heatmap of microcrack area (%) showing time-dependent changes in surface crack density, quantified as the percentage of segmented crack area relative to the total region of interest (ROI). (C) Comparative microcrack area at Day 56. MZ01 exhibits excellent surface stability with a significantly lower microcrack rate compared to WE43 and ZM115. (D) Heatmap of Mg volume loss (%) showing time-dependent volume changes, calculated from micro-CT data and expressed as the remaining volume percentage relative to Day 0 (100%). Data are expressed as mean ± standard deviation. SEM, scanning electron microscope; m-CT, micro-computed tomography; $^{**}p < 0.01$, $^{***}p < 0.001$.

long-term biological safety risks associated with rare-earth element accumulation, while achieving a favorable degradation and healing balance.

3.9. Ex-vivo micro-CT findings of microtube samples

Ex vivo micro-CT enabled non-destructive and safe quantitative evaluation of the overall microtube morphology and volume of the

remaining Mg alloy. The reconstructed CT images demonstrated progressive morphological deformation and material loss over time in all study groups, including tube wall thinning and irregular contour development. Consistent with the degradation behavior observed in the FE-SEM images, volumetric measurements revealed a clear time-dependent reduction in microtube volume. In particular, the magnitude and rate of volume loss differed among WE43, MZ01, and ZM115, indicating distinct biodegradation profiles for each. The mean percentage of volume loss in the MZ01 group (92.89 ± 1.19%) was higher than that in the WE43 (89.34 ± 1.21%) and ZM115 (90.31 ± 4.76%) groups, with no significant differences between the groups (Fig. 2D and Fig. S14). Micro-CT-based volume quantification provides an integrated measure of biodegradation that accounts for generalized corrosion and localized material loss. When interpreted alongside SEM crack analysis, micro-CT helps distinguish whether an alloy primarily undergoes gradual uniform thinning or exhibits more aggressive localized breakdown. The consistency between micro-CT volume loss, and SEM findings strengthens the internal validity of the degradation assessment approach used in this study.

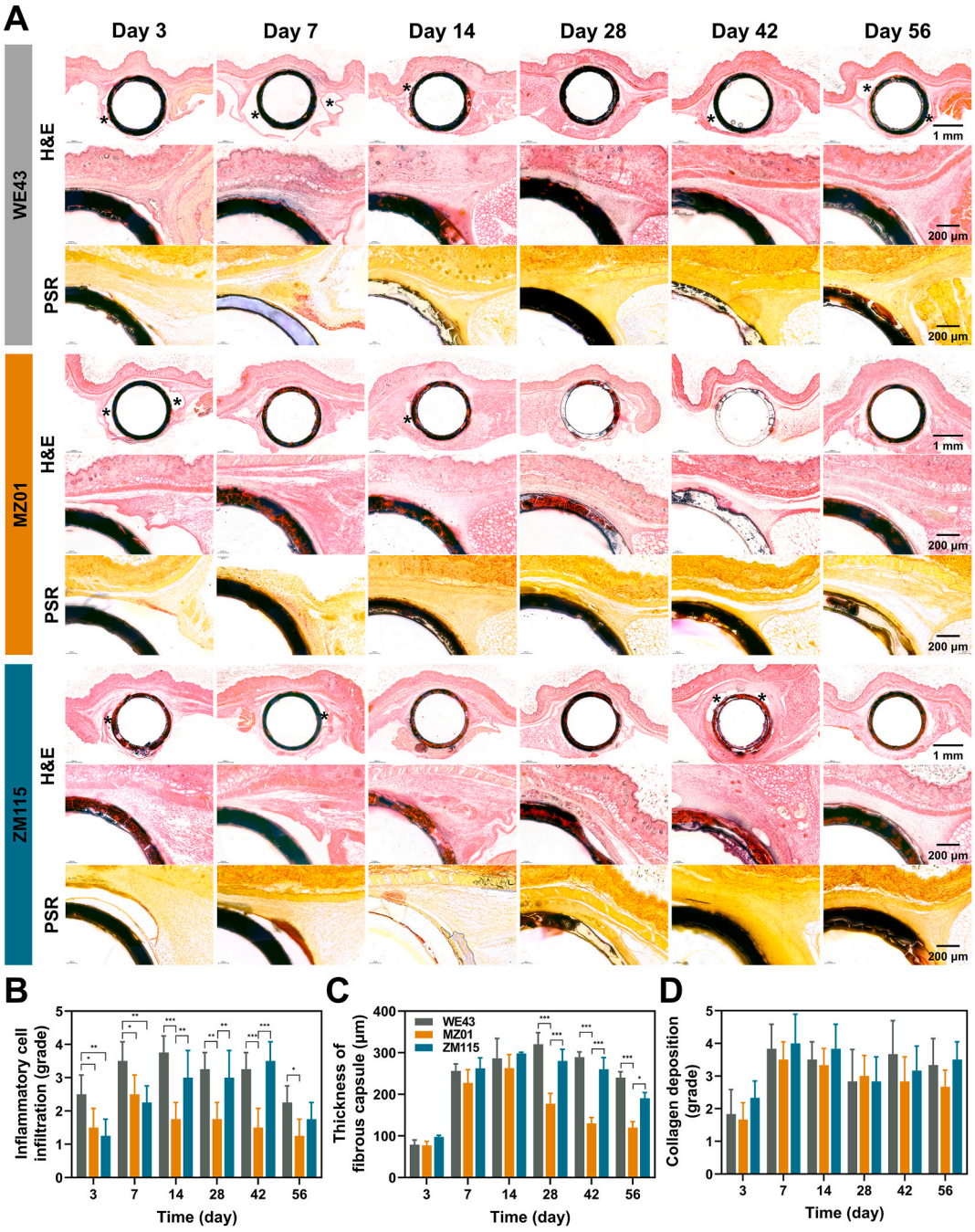

Fig. 3. Histological evaluation of Mg microtubes and surrounding tissue following subcutaneous implantation. (A) Representative hematoxylin and eosin (H&E; ×3 and ×20) and picrosirius red (PSR; ×20) stained images of tissue surrounding WE43, MZ01, and ZM115 microtubes over 56 days (scale bar = 1 mm for ×3). Gas cavities (asterisks) were observed at selected time points. Graphs showing time-dependent changes in histological parameters, including (B) inflammatory cell infiltration, (C) fibrous capsule formation, and (D) collagen deposition. (For interpretation of the references to color in this figure legend, the reader is referred to the Web version of this article.)

3.10. Histological findings of the extracted microtube and surrounding tissues

Representative histological findings are presented in Fig. 3 and Table S7 H&E staining showed that microtube-implanted tissues in all groups developed a foreign body–type tissue response characterized by inflammatory cell infiltration and fibrous capsule formation. The early phase of the inflammatory cell infiltration was prominent adjacent to the implanted microtubes at Day 7. The mean inflammatory cell infiltration in the MZ01 group was significantly lower than that in the WE43 ($p < 0.001$) and ZM115 ($p < 0.01$) groups. The release of early local degradation products from Mg implants, which peaks on Day 3, induces a robust inflammatory response [53]. The gas cavity formation was observed in all groups at Day 7, and the gas cavity was maintained in the WE43 and ZM115 groups until Day 42 (Fig. S15 and Table S7). Accumulated gas cavities can block normal blood flow and damage surrounding tissues, which may limit the use of Mg in clinical settings [54]. Gas cavity formation involves the formation of hydrogen (H_2) gas cavities due to the reaction products of Mg and is a major obstacle to the use of Mg in clinical applications [55]. Additionally, the gas pockets created can delay the tissue healing process and are a major cause of tissue inflammatory responses [56]. Therefore, the resolution of gas cavities on Day 14 in the MZ01 group may have promoted the transition from the acute inflammatory phase to the tissue remodeling phase, whereas the persistent presence of gas cavities in the WE43 and ZM115 groups may have prolonged the inflammatory environment. The thickness of the fibrous capsule also enhanced time-dependent modulation without significant differences between the study groups until Day 14, and then gradually decreased in all groups, reflecting the dynamic interplay between ongoing Mg degradation, corrosion product deposition, and tissue remodeling [57]. The mean thickness of the fibrous capsule in the MZ01 group was significantly lower than that in the WE43 and ZM115 groups at Day 14 (all $p < 0.05$). Mg implants induced an initial inflammatory response with the maximum release of degradation products around Day 3, and the inflammation gradually subsided as the implant surface stabilized [53]. Consistent with this phenomenon, the MZ01 group successfully transitioned from an initial stage to a stabilized and thinner fibrous membrane. In contrast, the WE43 and ZM115 groups exhibited slower decrease in thickness accompanied by sustained inflammatory responses. This prolonged reaction may be attributable to accelerated degradation with continuous H_2 evolution, which can interfere with normal physiological wound-healing regulation. PSR staining revealed collagen deposition around the implants, with progressive accumulation and maturation patterns gradually increasing and then decreasing over time, with no significant intergroup differences at any time point. This temporal pattern is consistent with previous reports showing that type 1 collagen deposition around Mg implants typically peaks at 1–2 weeks and decreases markedly by 4 weeks as inflammation subsides and vascularization progresses [53,58]. Therefore, these findings indicate that none of the three alloys affected the overall healing process. WE43, MZ01, and ZM115 demonstrated time-dependent biodegradation accompanied by a measurable tissue response. The multimodal approach used here provides complementary information: gross inspection identifies gas cavity formation and macroscopic changes, SEM quantifies surface-level degradation, micro-CT measures volumetric loss, and histology characterizes the biological response and tissue remodeling. In particular, concordant trends across these endpoints indicate that alloy composition influences the degradation kinetics and the peri-implant response in the mouse subcutaneous environment. These results underscore the importance of optimizing Mg alloy chemistry to achieve predictable biodegradation while minimizing adverse local tissue reactions.

3.11. Procedural outcomes, follow-up angiography, OCT, and micro-CT findings

Stent placement was successfully performed in both iliac arteries of the rabbits according to the designed timeline (Fig. 4A and B). All rabbits survived until their designated time of euthanasia, and no systemic adverse events, including body weight loss, were observed during the follow-up period (Fig. S16). Angiography before stent placement confirmed the location of the target vessel, and immediate post-procedural angiography demonstrated preserved stent patency and positioning in all cases. During the follow-up period, angiography showed sustained vessel patency across the three groups, with no evidence of acute thrombosis, stent migration, or flow-limiting dissection (Fig. 4C and Table S8). The percentages of luminal patency within the stented iliac artery diameter gradually decreased over time in all groups. The mean percentage of luminal patency in the MZ01 group was relatively higher than that in the WE43 and ZM115 groups at Days 14, 28, and 56, respectively (Fig. 4D). No significant differences were seen between the study groups at any time point, suggesting that vascular healing and neointimal response were comparable across the alloys. Angiography provides a clinically relevant assessment of patency and flow, but it is limited in resolving intraluminal tissue response and neointimal architecture. Therefore, angiographic findings were interpreted together with OCT and histology to distinguish simple luminal remodeling from true neointimal hyperplasia. OCT imaging was successfully performed at each follow-up time point, enabling high-resolution visualization of the luminal boundary and neointimal coverage within the stented segment. The neointimal thickness and the stenotic area were lowest in the MZ01 group at all time points, and no significant differences were observed between the study groups at Day 56 (Fig. 4E). The stenotic area was relatively less in the MZ01 group throughout the study period, reaching $28.1 \pm 5.2\%$ at Day 56, while those in the WE43 and ZM115 groups were $33.7 \pm 1.5\%$ and $33.9 \pm 2.0\%$, respectively (Fig. 4F). The time course observed on OCT is consistent with expected vascular healing after stent placement, where early neointimal formation reflects smooth muscle cell activation and extracellular matrix deposition, followed by later maturation and remodeling [42]. The mechanical strength of Mg-Zn series alloys increases by adding Zn to Mg [59]. Additionally, Zn ions generated during the decomposition process inhibit the activity of vascular smooth muscle cells, suggesting that neointimal proliferation may be inhibited by zinc ions [28]. These findings suggest that, despite the absence of RE elements, Mg-ZN alloys, especially MZ01, possess lumen-maintaining properties and do not cause excessive neointimal hyperplasia due to degradation and toxicity in a rabbit iliac artery model.

Beyond evaluating intraluminal tissue response, OCT and micro-CT findings also provided crucial insights into the biodegradation and structural integrity of the stents. Biodegradable metal stents such as the Mg stent are difficult to observe via fluoroscopy due to their lack of radiopacity, but the width of the strut can be observed in OCT and is used for approximate biodegradation evaluation [60]. On Day 56, struts were identified in all groups via OCT, but the boundaries were the most distinct in the MZ01 group, indicating that among the Mg–Zn alloys, MZ01 maintained its stent structure relatively well at the end of the study. The detailed morphology of the degraded stents was further observed via micro-CT. An overall reduction in strut thickness was observed in all groups; however, while WE43 and ZM115 lost their stent structure due to corrosion, MZ01 retained its shape relatively well.

Despite the favorable vascular response and biocompatibility of the Mg-Zn alloys, this study has some limitations. First, the relatively small sample size, especially small porcine cohort, may have limited the statistical power to detect subtle differences between the groups, although MZ01 showed a numerical trend toward a reduced neointimal area. Second, using a healthy rabbit and porcine models, non-atherosclerotic vessels, does not fully reproduce the calcified, inflamed, and mechanically heterogeneous environment of diseased coronary arteries. While

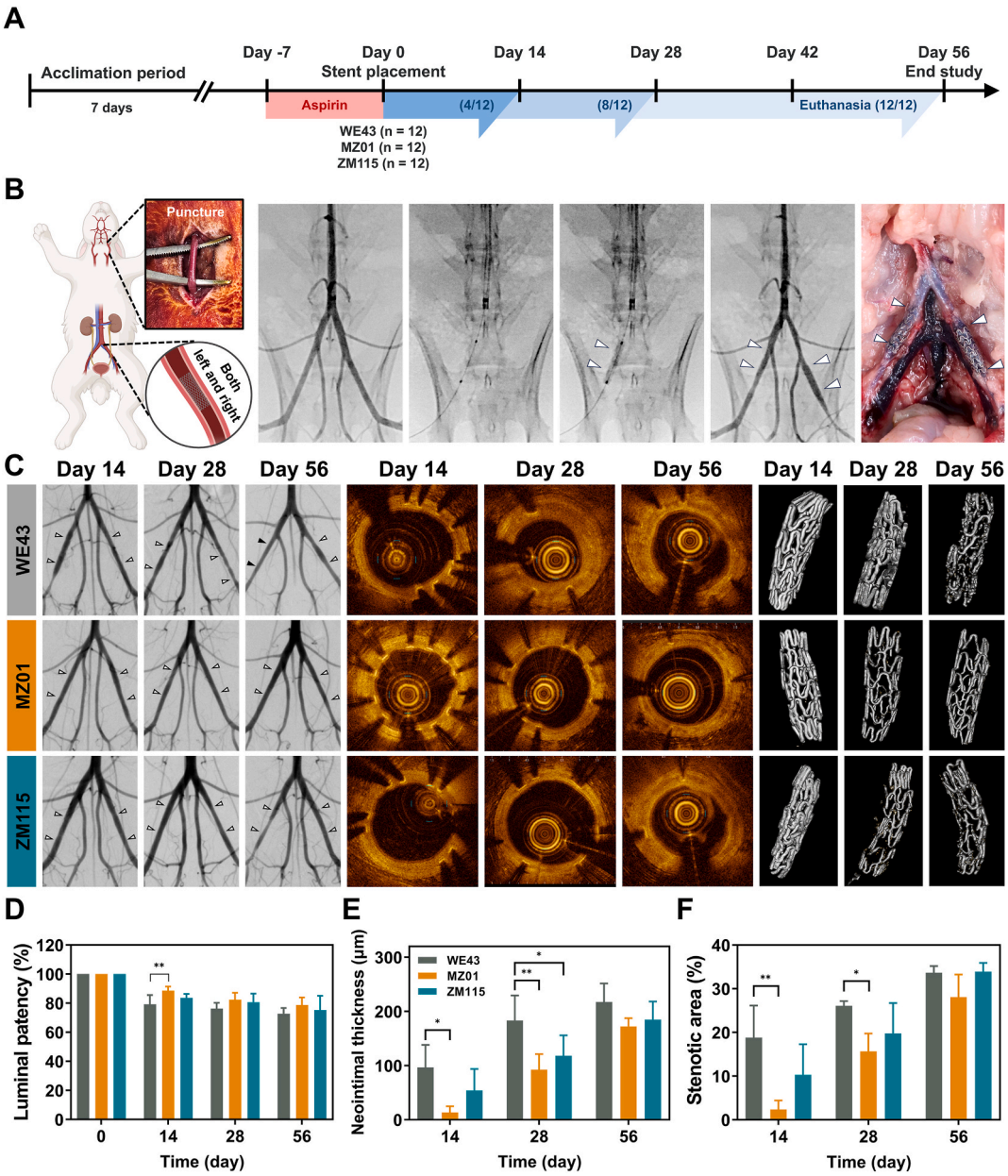

Fig. 4. *In vivo* evaluation of Mg stents in a rabbit iliac artery model. (A) Schematic illustration of the 56-day follow-up period, including aspirin administration, stent placement (Day 0), and serial euthanasia time points. (B) Technical steps of stent placement in the rabbit iliac artery. The Mg stent (white arrowheads) was not visible under fluoroscopic guidance, so its location was determined based on the radiopaque marker on the balloon catheter. After all experiments were completed, the status of stent placement in the rabbit iliac artery was visually confirmed. (C) Representative angiography, optical coherence tomography (OCT), and micro-CT images for the WE43, MZ01, and ZM115 groups over 56 days. The images indicated sustained luminal patency and progressive neointimal coverage. Quantitative analysis of (D) luminal patency (%), (E) neointimal thickness (μm), and (F) stenotic area (%). Data are expressed as mean ± standard deviation.

this allowed us to evaluate the intrinsic reaction and degradation behavior of alloy materials in a vascular environment, future research aims to evaluate stents coated with antiproliferative drugs in atherosclerotic and calcified vascular animal models, aligned with standard cardiovascular treatment. Although multiple animal models were used to assess different aspects of alloy performance, each model was selected for a distinct purpose, including biodegradation and local tissue response, vascular biological responses, and large-animal technical feasibility. This stepwise approach was intended to obtain complementary information while minimizing unnecessary animal use in accordance with the 3Rs principles. Finally, the anatomical differences between the rabbit iliac artery and human coronary arteries must be considered. Variations in vessel diameter, blood flow hemodynamics, and mechanical stress levels mean that the lumen-maintaining properties observed here require further validation in larger animal models or clinical settings. Although a preliminary implantation in a pig coronary artery model provided supportive evidence in this regard, the currently underpowered porcine groups and limited number of animals restrict definitive conclusions. Therefore, cohort studies with larger and sufficient sample sizes long-term follow-up are necessary to assess scaffold integrity, vascular remodeling, late degradation, and safety.

3.12. *Histological findings in the rabbit iliac artery*

The surgical exploration of the rabbit iliac artery was performed successfully. Histological findings are presented in Fig. 5 and Fig. S17 and summarized in Table S9. H&E staining demonstrated that all stent struts were surrounded by progressive neointimal tissue formation

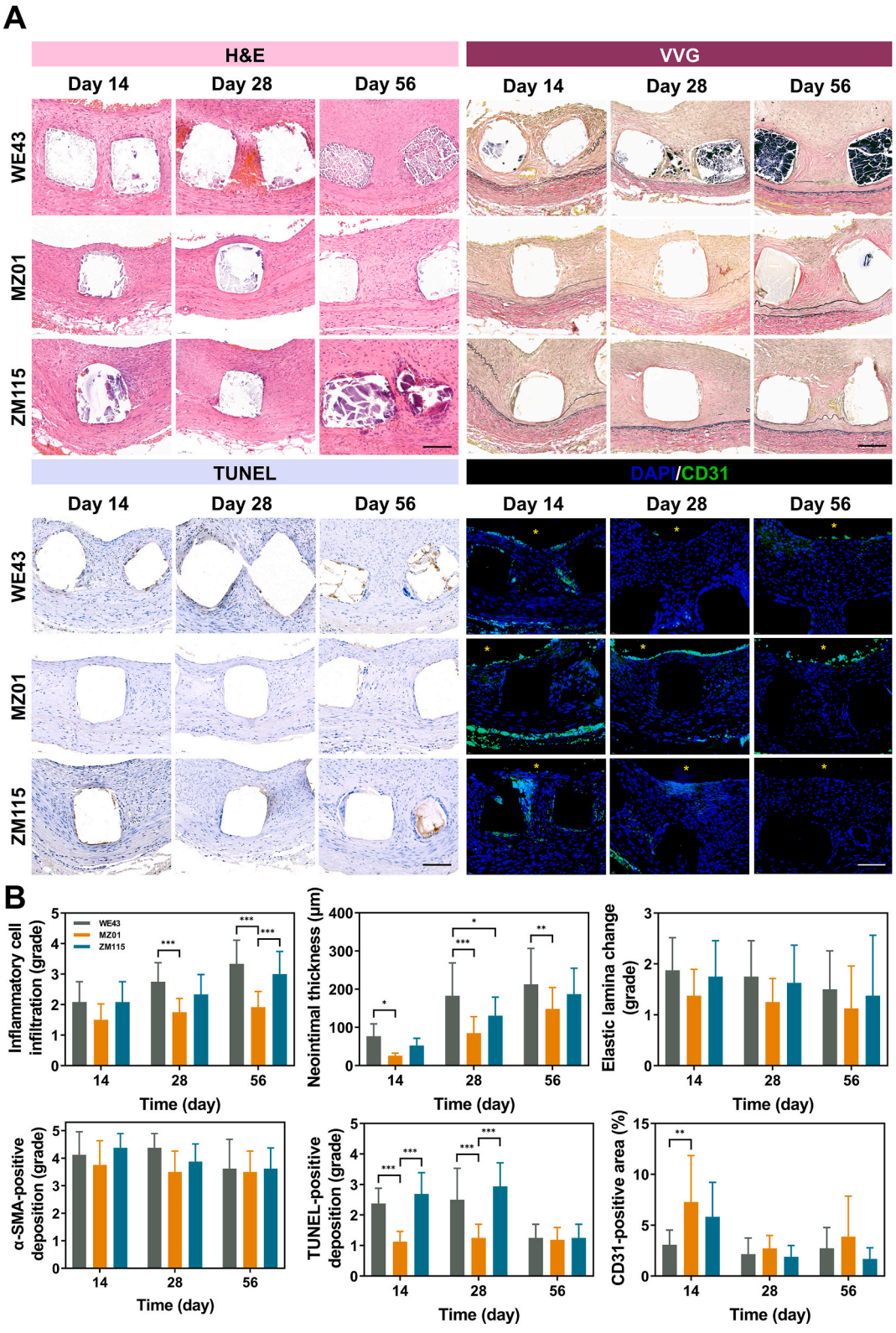

Fig. 5. Representative histological findings. (A) Representative microscopic images of H&E, VVG, TUNEL, and CD31 staining at 30× magnification (Scale bar = 100 μm). (B) Statistical graphs of histological examination. Data were expressed as mean ± standard deviation. H&E, Hematoxylin and eosin; VVG, Verhoeff-Van Gieson; TUNEL, terminal deoxynucleotidyl transferase-mediated dUTP nick-end labeling; α-SMA, alpha smooth muscle actin; $^{*}p < 0.05$, $^{**}p < 0.01$, $^{***}p < 0.001$.

across all groups and time points. Inflammatory cell infiltration showed a time-dependent increase in all groups, with WE43 exhibiting the highest degree of infiltration throughout the study period. The MZ01 group showed consistently lower inflammatory cell infiltration compared to WE43, with significant differences at Day 28 ($p < 0.001$) and Day 56 ($p < 0.001$). ZM115 had a non-significantly lower degree of inflammatory cell infiltration than WE43, and, on Day 56, a significantly higher level of inflammatory cell infiltration compared to MZ01 ($p < 0.001$). Neointimal thickness increased progressively over time in all groups. MZ01 exhibited significantly thinner neointima compared to WE43 at Day 14 ($p < 0.05$), Day 28 ($p < 0.001$), and Day 56 ($p < 0.01$), while ZM115 showed intermediate values without a significant difference from either group at most time points. VVG staining results showed changes in the elastic plates in all groups, and the degree of arterial damage was similar at all time points without significant differences between groups. The histological findings are consistent with and complementary to the angiographic and OCT results, collectively indicating that MZ01 induces a significantly attenuated vascular inflammatory response compared to the RE-containing WE43 alloy. The progressive increase in neointimal thickness observed across all groups reflects the expected vascular healing response following stent implantation, characterized by smooth muscle cell migration, extracellular matrix deposition, and subsequent remodeling [59]. The markedly thinner neointima in the MZ01 group suggests that the more controlled degradation profile of this alloy, as evidenced by the subcutaneous model findings, translates into a reduced inflammatory stimulus in the vascular environment.

3.13. *Immunohistochemical and immunofluorescent findings in the rabbit iliac artery*

Immunohistochemical and immunofluorescent findings are presented in Fig. 5, Fig. S18, S19 and summarized in Table S9. The α-SMA positive deposition, which reflects the smooth muscle cell content in the neointima [61,62], was high and similar in all three groups at all time points, but was relatively low in MZ01, similar to neointimal thickness (Fig. S18). On Days 14 and 28, the WE43 and ZM115 groups showed significantly higher TUNEL-positive deposition compared to the MZ01 group (all $p < 0.001$). TUNEL-positive areas were observed mainly in the neointimal region around the stent strut, suggesting that apoptosis due to stent degradation was activated [63]. On Day 56, TUNEL-positive deposition was significantly reduced in all groups, and the differences between groups disappeared. These findings suggest that, consistent with the *in vitro* cell viability results, WE43 and ZM115 exhibited rapid degradation early on compared to MZ01, and indicate that cytotoxic stress was alleviated on Day 56. The CD31-positive area revealed that MZ01 exhibited the highest on Day 14, which was significantly higher than that in WE43 ($p < 0.01$). ZM115 exhibited a median value (Fig. S19). On Days 28 and 56, the CD31-positive regions became similar between the groups with no significant difference. In addition, CD31 was rarely observed around the stent support, suggesting that the increase in pH due to stent degradation inhibited endothelial cell growth [64]. Therefore, the low TUNEL-positive deposition and high CD31-positive area in the MZ01 group at the initial stage indicated lower cytotoxicity compared to WE43 and ZM115. These results are consistent with *in vitro* cytotoxicity findings, and when considered in conjunction with micro-CT results from mice and rabbits, the slow degradation rate of MZ01 suggests that it relatively suppresses cytotoxicity caused by pH elevation or high concentrations of metal ions.

3.14. *Preliminary evaluation of MZ01 stents in a porcine coronary artery model*

In this preliminary evaluation, the MZ01 stent, which demonstrated relatively superior performance in mouse subcutaneous and rabbit iliac artery models, was implanted into the coronary arteries of three pigs. The stent used was identical in specifications to that used in rabbits, with no additional modifications. Stent placement was technically successful in all vessels (6/6) without procedure-related adverse events such as dissection or thrombosis (Fig. 6A and B). All animals survived until the designated euthanasia time points without experiencing weight loss. Follow-up angiography indicated a gradual decrease in luminal diameter over time, from $78.95 \pm 9.20\%$ at Day 14 to $67.82 \pm 6.83\%$ at Day 28 and $67.06 \pm 9.08\%$ at Day 56, with no evidence of stent thrombosis or flow-limiting occlusion, and no significant differences were observed (Fig. 6C and D). Correspondingly, OCT-derived neointimal thickness and stenotic area increased progressively over the follow-up period, with neointimal thickness reaching 132.50 ± 61.85 μm at Day 14, 240.00 ± 100.33 μm at Day 28, and 297.50 ± 39.48 μm at Day 56 (Day 14 vs. Day 56, $p < 0.05$), and stenotic area increasing $22.90 \pm 9.03\%$ at Day 14, $33.23 \pm 10.19\%$ at Day 28, and $38.88 \pm 6.88\%$ at Day 56 (all $p =$ ns). H&E staining of the stented coronary segments revealed a time-dependent pattern of inflammatory cell infiltration, increasing from Day 14 (1.25 ± 0.46) to Day 28 (2.38 ± 0.52, $p < 0.01$) and then tended to decrease by Day 56 (1.75 ± 0.71) (Fig. 6C and D). This early increase followed by partial resolution is consistent with the transient inflammatory response associated with the initial burst of Mg degradation products, as similarly observed in the mouse subcutaneous and rabbit iliac artery models, suggesting that the degradation-driven inflammatory profile of MZ01 observed in smaller animal models is at least qualitatively reproducible in a pig coronary environment. Despite the limitations in sample size, the study demonstrates the technical feasibility and short-term safety of MZ01 stents in pig coronary arteries. This is evidenced by the absence of procedure-related death, thrombosis, or occlusion, as well as sustained luminal patency and a manageable inflammatory response over 56 days. The anatomical and hemodynamic environment of pig coronary arteries is significantly more similar to human coronary circulation than the rabbit iliac artery, directly addressing one of the limitations identified in the rabbit iliac artery study. To date, most preclinical and clinical studies of biodegradable Mg stents have focused on Mg alloys containing RE elements, raising concerns regarding their potential long-term biosafety and motivating the development of RE-free Mg alloys [65,66]. Previous studies on RE-free Mg–Zn-based alloys have primarily focused on bulk material properties, *in vitro* degradation, cytocompatibility, or orthopedic applications [59,67]. In contrast, the present study comprehensively evaluated the performance of Mg-Zn-based alloys by integrating *in vitro* characterization, *in vivo* implantation, and evaluation under physiologically relevant cardiovascular conditions. Therefore, compared with previously reported RE-free Mg–Zn alloys, the major contribution of the present study lies in establishing an integrated mechanistic framework linking stent deployment characteristics, degradation behavior, local tissue response, and vascular healing. Nevertheless, direct comparison with previous studies should be made cautiously, because Mg–Zn alloy performance is strongly affected by composition, processing conditions, surface treatment, stent geometry, and implantation environment.

4. Conclusion

Three biodegradable Mg alloy (WE43, MZ01, and ZM115) stents and microtubes were successfully fabricated with consistent geometry and adequate surface integrity for crimping and deployment to evaluate the technical feasibility and safety of using an Mg alloy as a cardiovascular stent in mouse subcutaneous microtube implantation and rabbit iliac artery stent models. In the mouse subcutaneous model, all Mg microtubes exhibited time-dependent biodegradation accompanied by a typical foreign body response. Although transient hydrogen gas cavities were observed early after implantation, the MZ01 group showed smaller and more rapidly resolving gas cavities, and demonstrated more uniform surface degradation compared with WE43 and ZM115. Quantitative FE-SEM crack analysis further indicated that MZ01 had the lowest crack area fraction at late time points, suggesting a more controlled

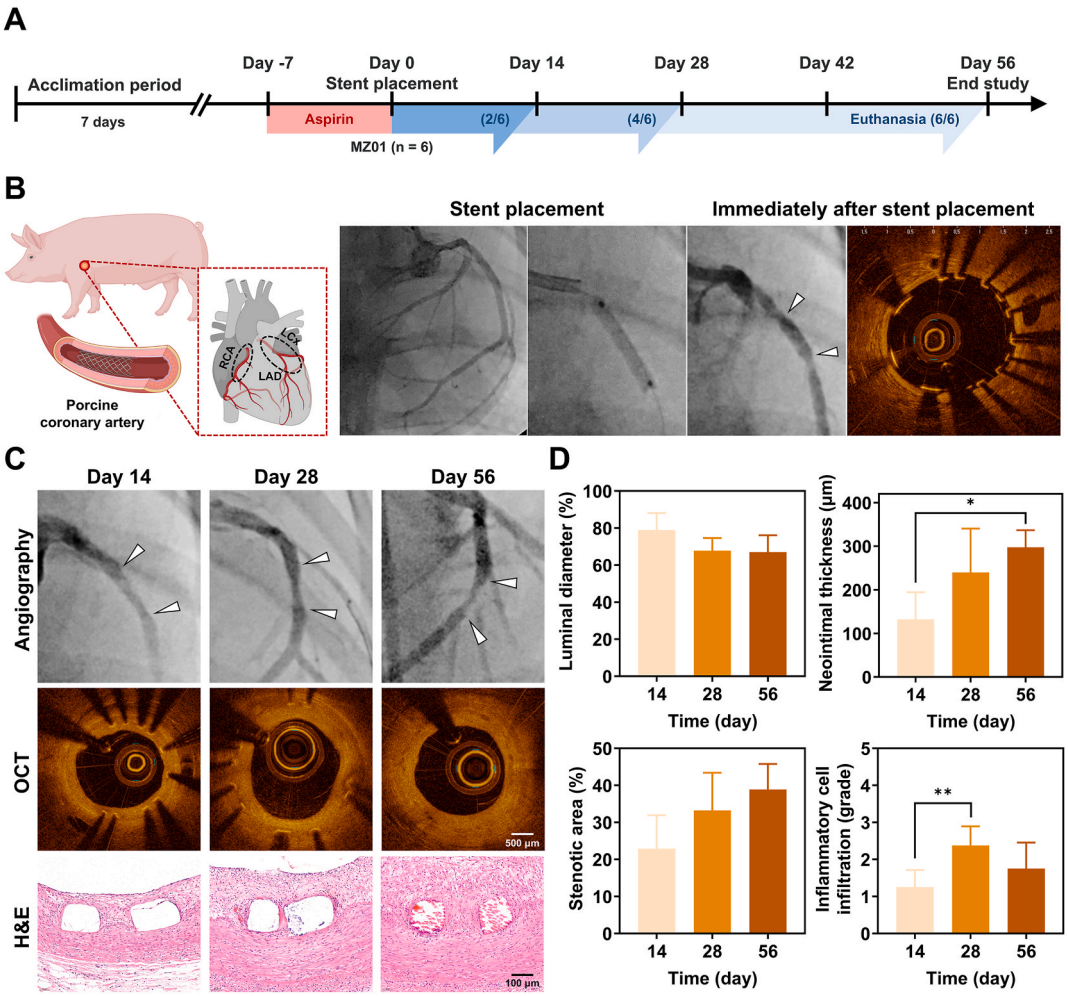

Fig. 6. Preliminary evaluation of MZ01 stents in a porcine coronary artery model. (A) Schematic illustration of the experimental timeline. (B) Schematic illustration of stent placement in the porcine coronary arteries is shown, with two stents per minipig placed in the left anterior descending artery (LAD), left circumflex artery (LCx), and right coronary artery (RCA). The technical steps of stent placement are demonstrated via angiography and OCT. (C) Representative images from angiography, OCT, and H&E-stained histological sections of stented coronary arteries at Days 14, 28, and 65 after stent placement. (D) Quantitative analyses of luminal diameter (%), neointimal thickness (μm), stenotic area (%), and inflammatory cell infiltration grade measured at Days 14, 28, and 56. Data are expressed as mean ± standard deviation. OCT, optical coherence tomography; H&E, hematoxylin and eosin; $*p < 0.05$, $**p < 0.01$.

degradation profile. Histologically, all groups showed progressive fibrous capsule formation and collagen remodeling with no significant differences in collagen deposition among alloys, indicating that none of the tested alloys adversely altered the overall healing trajectory in subcutaneous tissue. In the rabbit iliac artery model, stent placement was technically successful and follow-up angiography demonstrated maintained patency without thrombosis or flow-limiting complications throughout the study period. Angiographic luminal diameter did not differ significantly among groups at any time point, suggesting comparable macroscopic lumen maintenance. OCT of vascular healing demonstrated gradual signal attenuation behind struts consistent with progressive biodegradation. Neointimal thickness and stenotic area were broadly comparable among alloys, with MZ01 tending toward lower stenotic area at late follow-up, supporting a favorable balance between scaffold resorption and vascular repair. Collectively, these findings indicate that the RE-free Mg–Zn alloy MZ01 provides biodegradation and biocompatibility profiles comparable to the clinically used WE43 alloy, including more uniform degradation, reduced early gas-associated tissue reactions, and acceptable vascular healing without excessive neointimal hyperplasia. A preliminary implantation of MZ01 stents in a pig coronary artery model further showed technically successful placement, sustained luminal patency, and a self-limited inflammatory response over 56 days without thrombosis or occlusion, lending additional support to its feasibility in an anatomical environment closer to the human coronary circulation. Therefore, MZ01 represents a promising RE-free material platform for next-generation biodegradable Mg stents, warranting further optimization of degradation-controlled design to improve long-term structural integrity and minimize fracture-related events during the resorption phase.

CRediT authorship contribution statement

Yubeen Park: Writing – original draft, Visualization, Methodology, Formal analysis, Conceptualization. **Yerin Ha:** Writing – review & editing, Validation, Investigation, Data curation. **Hyung Jin Roh:** Data curation, Resources, Writing – review & editing. **Hyun Lee:** Formal analysis, Methodology, Writing – review & editing. **Seung Jin Eo:** Writing – review & editing, Validation, Investigation, Data curation. **Do-Yoon Kang:** Writing – review & editing, Investigation, Formal analysis. **Nayoung Lee:** Visualization, Formal analysis. **Hyun-Do Jung:** Resources, Investigation. **Jun-Kyu Park:** Resources, Funding acquisition. **Kang-Sik Lee:** Project administration, Funding acquisition. **Yu-Chan Kim:** Writing – review & editing, Funding acquisition. **Hwa-Chul Jung:** Resources, Project administration. **Joung Sik Suh:** Validation, Investigation, Conceptualization. **Jung-Hoon Park:** Writing – review & editing, Visualization, Supervision, Methodology, Funding acquisition,

Conceptualization.

Declaration of generative AI and AI-assisted technologies in the manuscript preparation process

During the preparation of this work, the authors used ChatGPT and BioRender to assist in creating schematic illustrations. After using these tools, the authors reviewed and edited the illustrations as needed and take full responsibility for the content and illustrations of the published article.

Funding sources

This work was supported by Nano·Material Technology Development Program through the National Research Foundation of Korea (NRF) grant funded by the Korea government (MSIT) (RS-2022-NR068191).

Declaration of competing interest

The authors declare the following financial interests/personal relationships which may be considered as potential competing interests: Jung-Hoon Park reports financial support was provided by National Research Foundation of Korea. If there are other authors, they declare that they have no known competing financial interests or personal relationships that could have appeared to influence the work reported in this paper.

Acknowledgements

The authors would like to acknowledge the following individuals or institutions for their expertise and assistance throughout all aspects of our study, as well as their assistance in writing the manuscript: the Biomedical Engineering Research Center at Asan Medical Center for technical assistance.

Appendix A. Supplementary data

Supplementary data to this article can be found online at https://doi.org/10.1016/j.biomaterials.2026.124691.

Data availability

Data will be made available on request.

References

[1] R.A. Sahu, A. Nashine, A. Mudey, S.A. Sahu, R. Prasad, Cardiovascular stents: types and future landscape, Cureus 15 (8) (2023) e43438.
[2] J. Wiebe, H.M. Nef, C.W. Hamm, Current status of bioresorbable scaffolds in the treatment of coronary artery disease, J. Am. Coll. Cardiol. 64 (23) (2014) 2541–2551.
[3] M. Bukka, P.J. Rednam, M. Sinha, Drug-eluting balloon: design, technology and clinical aspects, Biomed. Mater. 13 (3) (2018) 032001.
[4] G.G. Stefanini, R.A. Byrne, S. Windecker, A. Kastrati, State of the art: coronary artery stents – past, present and future, EuroIntervention 13 (6) (2017) 706–716.
[5] D.S. Park, M.H. Jeong, Y.J. Jin, M.H. Na, D.S. Sim, M. Kim, K.H. Cho, D.Y. Hyun, S. Oh, J.H. Kim, K.S. Lim, J.K. Park, H.K. Kim, Y.J. Hong, J.H. Kim, Y. Ahn, J. H. Kim, Preclinical evaluation of an everolimus-eluting bioresorbable vascular scaffold via a long-term rabbit iliac artery model, Tissue Eng. Regen. Med. 20 (2) (2023) 239–249.
[6] J. Bukala, P.P. Buszman, J. Małachowski, L. Mazurkiewicz, K. Sybilski, Experimental tests, FEM constitutive modeling and validation of PLGA bioresorbable polymer for stent applications, Materials 13 (8) (2020) 2003.
[7] X. Cao, G. Chen, Y. Fan, Y. Shen, M. Li, Y. Zheng, Development and translation of biodegradable metal stents: from heart to brain, Regen. Biomater. 13 (2026) rbag079.
[8] H. Jinnouchi, S. Torii, A. Sakamoto, F.D. Kolodgie, R. Virmani, A.V. Finn, Fully bioresorbable vascular scaffolds: lessons learned and future directions, Nat. Rev. Cardiol. 16 (5) (2019) 286–304.
[9] S.A. Park, S.J. Lee, K.S. Lim, I.H. Bae, J.H. Lee, W.D. Kim, M.H. Jeong, J.-K. Park, In vivo evaluation and characterization of a bio-absorbable drug-coated stent fabricated using a 3D-printing system, Mater. Lett. 141 (2015) 355–358.
[10] J. Fu, Y. Su, Y.-X. Qin, Y. Zheng, Y. Wang, D. Zhu, Evolution of metallic cardiovascular stent materials: a comparative study among stainless steel, magnesium and zinc, Biomaterials 230 (2020) 119641.
[11] Z.Q. Zhang, Y.X. Yang, J.A. Li, R.C. Zeng, S.K. Guan, Advances in coatings on magnesium alloys for cardiovascular stents - a review, Bioact. Mater. 6 (12) (2021) 4729–4757.
[12] G. Kumar, S. Preetam, A. Pandey, N. Birbilis, S. Al-Saadi, P. Pasbakhsh, M. Zheludkevich, P. Balan, Advances in magnesium-based bioresorbable cardiovascular stents: surface engineering and clinical prospects, J. Magnesium Alloys 13 (3) (2025) 948–981.
[13] S. Wang, C. Du, X. Shen, X. Wu, S. Ouyang, J. Tan, J. She, A. Tang, X. Chen, F. Pan, Rational design, synthesis and prospect of biodegradable magnesium alloy vascular stents, J. Magnesium Alloys 11 (9) (2023) 3012–3037.
[14] L. Mao, L. Shen, J. Chen, X. Zhang, M. Kwak, Y. Wu, R. Fan, L. Zhang, J. Pei, G. Yuan, C. Song, J. Ge, W. Ding, A promising biodegradable magnesium alloy suitable for clinical vascular stent application, Sci. Rep. 7 (2017) 46343.
[15] J. Xu, J. Zou, D. Zhang, K. Zhang, Y. Qi, C. Yan, E.-S. Lee, Q. Jia, C. Ma, H.B. Jiang, In vitro assays and development strategies for magnesium-based biodegradable cardiovascular stent: a decade of review, Prog. Mater. Sci. 156 (2026) 101541.
[16] D. Liu, K. Yang, S. Chen, Development and future trends of protective strategies for magnesium alloy vascular stents, Materials (2024) 68.
[17] C.M. Campos, T. Muramatsu, J. Iqbal, Y.J. Zhang, Y. Onuma, H.M. Garcia-Garcia, M. Haude, P.A. Lemos, B. Warnack, P.W. Serruys, Bioresorbable drug-eluting magnesium-alloy scaffold for treatment of coronary artery disease, Int. J. Mol. Sci. 14 (12) (2013) 24492–24500.
[18] M. Haude, R. Erbel, P. Erne, S. Verheye, H. Degen, D. Böse, P. Vermeersch, I. Wijnbergen, N. Weissman, F. Prati, R. Waksman, J. Koolen, Safety and performance of the drug-eluting absorbable metal scaffold (DREAMS) in patients with de-novo coronary lesions: 12 month results of the prospective, multicentre, first-in-man BIOSOLVE-I trial, Lancet 381 (9869) (2013) 836–844.
[19] X. Chen, Y. Xia, S. Shen, C. Wang, R. Zan, H. Yu, S. Yang, X. Zheng, J. Yang, T. Suo, Y. Gu, X. Zhang, Research on the current application status of magnesium metal stents in human luminal cavities, J. Funct. Biomater. 14 (9) (2023).
[20] J. Bennett, Q. De Hemptinne, K. McCutcheon, Magmaris resorbable magnesium scaffold for the treatment of coronary heart disease: overview of its safety and efficacy, Expert Rev. Med. Dev. 16 (9) (2019) 757–769.
[21] J. Liu, D. Bian, Y. Zheng, X. Chu, Y. Lin, M. Wang, Z. Lin, M. Li, Y. Zhang, S. Guan, Comparative in vitro study on binary Mg-RE (Sc, Y, La, Ce, Pr, Nd, Sm, Eu, Gd, Tb, Dy, Ho, Er, Tm, Yb and Lu) alloy systems, Acta Biomater. 102 (2020) 508–528.
[22] F. Feyerabend, J. Fischer, J. Holtz, F. Witte, R. Willumeit, H. Drücker, C. Vogt, N. Hort, Evaluation of short-term effects of rare earth and other elements used in magnesium alloys on primary cells and cell lines, Acta Biomater. 6 (5) (2010) 1834–1842.
[23] S. Zhang, X. Zhang, C. Zhao, J. Li, Y. Song, C. Xie, H. Tao, Y. Zhang, Y. He, Y. Jiang, Y. Bian, Research on an Mg–Zn alloy as a degradable biomaterial, Acta Biomater. 6 (2) (2010) 626–640.
[24] Y. Chen, Z. Xu, C. Smith, J. Sankar, Recent advances on the development of magnesium alloys for biodegradable implants, Acta Biomater. 10 (11) (2014) 4561–4573.
[25] J. Kim, H. Kim, H.-C. Jung, J.S. Suh, J. Lee, Effect of extrusion ratio on mechanical and in vitro degradation properties of mg-zn-ca microtubes for biodegradable vascular stents, JOM 77 (6) (2025) 4393–4401.
[26] C. Zhang, J. Lin, N.-Y.T. Nguyen, Y. Guo, C. Xu, C. Seo, E. Villafana, H. Jimenez, Y. Chai, R. Guan, H. Liu, Antimicrobial bioresorbable Mg–Zn–Ca alloy for bone repair in a comparison study with Mg–Zn–Sr alloy and pure Mg, ACS Biomater. Sci. Eng. 6 (1) (2020) 517–538.
[27] J.-H. Dong, L.-L. Tan, Y.-B. Ren, K. Yang, Effect of microstructure on corrosion behavior of Mg–Sr alloy in Hank's solution, Acta Metall. Sin. 32 (3) (2018) 305–320.
[28] J. Ma, N. Zhao, D. Zhu, Bioabsorbable zinc ion induced biphasic cellular responses in vascular smooth muscle cells, Sci. Rep. 6 (2016) 26661.
[29] J.S. Suh, J.-Y. Kim, H.S. Kim, S.E. Lee, J. Kim, Effect of extrusion ratio on mechanical and biodegradation behavior of Mg–Zn–Mn–Sr alloy microtubes for biodegradable vascular stents, J. Magnesium Alloys 19 (2026).
[30] A. Al Hegy, R. Smith, E.R. Gauthier, J.E. Gray-Munro, Investigation of a cyanine dye assay for the evaluation of the biocompatibility of magnesium alloys by direct and indirect methods, Bioact. Mater. 5 (1) (2020) 26–33.
[31] T.Y. Pang, J.S. Kwok, C.T. Nguyen, K. Fox, Evaluating magnesium alloy WE43 for bioresorbable coronary stent applications, MRS Adv. 6 (3) (2021) 54–60.
[32] J.H. Seo, D.S. Won, H. Lee, S. Bang, H.S. Kang, J.Y. Gwon, C.H. Moon, J.W. Kim, Y. Park, M. Kang, D.Y. Lee, D. Lim, K. Yang, G.D. Cha, S.H. Lee, T.S. Jang, S. Kim, J. K. Park, J.H. Park, H.D. Jung, Mechanically robust biodegradable stents with theragenerative vascular responses via combined 3D printing and Janus nanoengineering, Adv. Sci. (Weinh.) 13 (34) (2026) e23965.
[33] S. Asghari, M.R. Shabgard, M. Shalvandi, F. Habibi, Surface quality evaluation of electrical discharge machined AZ31 magnesium alloy, Results Mater. 27 (2025) 100751.
[34] Y. Na, Y. Park, H. Lee, S.H. Kim, S. Bang, H.S. Kang, C.H. Moon, J.Y. Gwon, J. H. Seo, M.H. Kang, S.H. Lee, G.D. Cha, W. Park, H. Kang, J.H. Park, H.D. Jung, Joule-assisted nanotherapeutic urethral stent (JANUS) for spatiotemporal theragenerative treatment of urethral strictures, Adv. Funct. Mater. 35 (37) (2025).

[35] K.S. Lim, M.H. Jeong, I.H. Bae, J.K. Park, D.S. Park, J.M. Kim, J.H. Kim, D.L. Cho, D.S. Sim, K.H. Park, Y.J. Hong, Y. Ahn, Effect of atorvastatin-eluting stents in a rabbit iliac artery restenosis model, Chonnam Med. J. 49 (3) (2013) 118–124.
[36] K.S. Lim, J.-K. Park, M.H. Jeong, J.-W. Nah, D.-G. Kim, I.H. Bae, D.S. Park, J. M. Kim, J.H. Kim, D.L. Cho, D.S. Sim, K.-H. Park, Y.J. Hong, Y. Ahn, Comparison of sirolimus loaded PLGA-PEG Co-polymer coronary stent and bare metal stent in a porcine coronary restenosis model, Macromol. Res. 22 (6) (2014) 639–646.
[37] P.W. Radke, M. Joner, A. Joost, R.A. Byrne, S. Hartwig, G. Bayer, K. Steigerwald, E. Wittchow, Vascular effects of paclitaxel following drug-eluting balloon angioplasty in a porcine coronary model: the importance of excipients, EuroIntervention 7 (6) (2011) 730–737.
[38] N. Stanford, M. Barnett, Effect of composition on the texture and deformation behaviour of wrought Mg alloys, Scr. Mater. 58 (3) (2008) 179–182.
[39] N. Stanford, The effect of calcium on the texture, microstructure and mechanical properties of extruded Mg–Mn–Ca alloys, Mater. Sci. Eng., A 528 (1) (2010) 314–322.
[40] N. Hort, Y. Huang, K.U. Kainer, Intermetallics in magnesium alloys, Adv. Eng. Mater. 8 (4) (2006) 235–240.
[41] K.-P. Liu, J.-L. You, S.-Y. Jian, Y.-H. Chang, C.C. Tseng, M.-D. Ger, Effect of electropolishing parameters of WE43 magnesium alloy on corrosion resistance of artificial plasma, J. Mater. Res. Technol. 26 (2023) 4989–5000.
[42] N. Gonzalo, P.W. Serruys, N. Piazza, E. Regar, Optical coherence tomography (OCT) in secondary revascularisation: stent and graft assessment, EuroIntervention 5 (Suppl D) (2009) D93–d100.
[43] E. Jablonska, J. Kubasek, D. Vojtech, T. Ruml, J. Lipov, Test conditions can significantly affect the results of in vitro cytotoxicity testing of degradable metallic biomaterials, Sci. Rep. 11 (1) (2021) 6628.
[44] D. Liu, K. Yang, S. Chen, Development and future trends of protective strategies for magnesium alloy vascular stents, Materials 17 (1) (2023).
[45] H. Mraied, W. Wang, W. Cai, Influence of chemical heterogeneity and microstructure on the corrosion resistance of biodegradable WE43 magnesium alloys, J. Mater. Chem. B 7 (41) (2019) 6399–6411.
[46] J.W. Freeman, P.B. Snowhill, J.L. Nosher, A link between stent radial forces and vascular wall remodeling: the discovery of an optimal stent radial force for minimal vessel restenosis, Connect. Tissue Res. 51 (4) (2010) 314–326.
[47] Y. Li, Y. Wang, Z. Shen, F. Miao, J. Wang, Y. Sun, S. Zhu, Y. Zheng, S. Guan, A biodegradable magnesium alloy vascular stent structure: design, optimisation and evaluation, Acta Biomater. 142 (2022) 402–412.
[48] D.B. Kim, H. Choi, S.M. Joo, H.K. Kim, J.H. Shin, M.H. Hwang, J. Choi, D.-G. Kim, K.H. Lee, C.H. Lim, S.K. Yoo, H.-M. Lee, K. Sun, A comparative reliability and performance study of different stent designs in terms of mechanical properties: foreshortening, recoil, radial force, and flexibility, Artif. Organs 37 (4) (2013) 368–379.
[49] D. Noviana, D. Paramitha, M.F. Ulum, H. Hermawan, The effect of hydrogen gas evolution of magnesium implant on the postimplantation mortality of rats, J. Orthop. Transl. 5 (2016) 9–15.
[50] C. Li, Y. Zhao, J. Liu, J. Xu, D. Guo, H. Zhang, X. Zhou, P. Yang, S. Zhang, Comparison of corrosion behavior of WE43 and AZ80 alloys in NaCl and Na2SO4 solutions, Crystals 13 (3) (2023).
[51] F. Zucchi, V. Grassi, A. Frignani, C. Monticelli, G. Trabanelli, Electrochemical behaviour of a magnesium alloy containing rare earth elements, J. Appl. Electrochem. 36 (2) (2005) 195–204.
[52] C. Yang, N. Gupta, H. Ding, C. Xiang, Effect of microstructure on corrosion behavior of WE43 magnesium alloy in As cast and heat-treated conditions, Metals 10 (11) (2020).
[53] H. Ben Amara, D.C. Martinez, F.A. Shah, A.J. Loo, L. Emanuelsson, B. Norlindh, R. Willumeit-Römer, T. Plocinski, W. Swieszkowski, A. Palmquist, O. Omar, P. Thomsen, Magnesium implant degradation provides immunomodulatory and proangiogenic effects and attenuates peri-implant fibrosis in soft tissues, Bioact. Mater. 26 (2023) 353–369.
[54] L. Xu, X. Liu, K. Sun, R. Fu, G. Wang, Corrosion behavior in magnesium-based alloys for biomedical applications, Materials 15 (7) (2022).
[55] A. Patil, S.H. Zaky, R. Chong, K. Verdelis, E. Beniash, In vivo study of self-assembled alkylsilane coated degradable magnesium devices, J. Biomed. Mater. Res. B Appl. Biomater. 107 (2) (2019) 342–351.
[56] D. Dziuba, A. Meyer-Lindenberg, J.M. Seitz, H. Waizy, N. Angrisani, J. Reifenrath, Long-term in vivo degradation behaviour and biocompatibility of the magnesium alloy ZEK100 for use as a biodegradable bone implant, Acta Biomater. 9 (10) (2013) 8548–8560.
[57] N. Adel, N. Stankovic, G. Cervantes, A. Gindi, L.M. Shawky, Skin wound healing following injecting hyaluronic acid rejuvenating complex, polycaprolactone, or combination therapy: an experimental study, J. Cosmet. Dermatol. 24 (5) (2025) e70221.
[58] J.F. White, J.A. Werkmeister, T. Bisucci, I.A. Darby, J.A. Ramshaw, Temporal variation in the deposition of different types of collagen within a porous biomaterial implant, J. Biomed. Mater. Res. 102 (10) (2014) 3550–3555.
[59] G.D. López, P.L. Williams, E. England, J. Wang, C. Boehlert, J. Llorca, M. Echeverry-Rendón, Mg-Zn-Ca alloys for biodegradable medical implants. Part I: effects of zinc and calcium on mechanical and corrosion behavior and cytocompatibility, Surf. Coating. Technol. 513 (2025) 132519.
[60] T.L. Slottow, R. Pakala, T. Okabe, D. Hellinga, R.J. Lovec, F.O. Tio, A.B. Bui, R. Waksman, Optical coherence tomography and intravascular ultrasound imaging of bioabsorbable magnesium stent degradation in porcine coronary arteries, Cardiovasc. Revascularization Med. 9 (4) (2008) 248–254.
[61] W. Zhao, X. Wang, K.H. Sun, L. Zhou, α-smooth muscle actin is not a marker of fibrogenic cell activity in skeletal muscle fibrosis, PLoS One 13 (1) (2018) e0191031.
[62] K.H. Sun, Y. Chang, N.I. Reed, D. Sheppard, α-Smooth muscle actin is an inconsistent marker of fibroblasts responsible for force-dependent TGFβ activation or collagen production across multiple models of organ fibrosis, Am. J. Physiol. Lung Cell. Mol. Physiol. 310 (9) (2016) L824–L836.
[63] M. Kollum, S. Kaiser, R. Kinscherf, J. Metz, W. Kübler, C. Hehrlein, Apoptosis after stent implantation compared with balloon angioplasty in rabbits, Arterioscler. Thromb. Vasc. Biol. 17 (11) (1997) 2383–2388.
[64] T. Shang, K. Wang, S. Tang, Y. Shen, L. Zhou, L. Zhang, Y. Zhao, X. Li, L. Cai, J. Wang, The flow-induced degradation and vascular cellular response study of magnesium-based materials, Front. Bioeng. Biotechnol. 10 (2022) 940172.
[65] J. Nicolas, C.A. Pivato, M. Chiarito, F. Beerkens, D. Cao, R. Mehran, Evolution of drug-eluting coronary stents: a back-and-forth journey from the bench to bedside, Cardiovasc. Res. 119 (3) (2023) 631–646.
[66] J. Zhu, X. Zhang, J. Niu, Y. Shi, Z. Zhu, D. Dai, C. Chen, J. Pei, G. Yuan, R. Zhang, Biosafety and efficacy evaluation of a biodegradable magnesium-based drug-eluting stent in porcine coronary artery, Sci. Rep. 11 (1) (2021) 7330.
[67] L. Weber, J. Horky, C. Riedmüller, C. Kampleitner, E. Acar, M. Fedel, C. Höchsmann, M. Eskinja, S. Mitsche, B. Mingler, L. Sajti, G. Mori, M. Bammer, I. Walter, S. Tangl, H. Bergmeister, B.K. Podesser, M. Enayati, A high-toughness, rare-earth-free magnesium alloy with excellent biocompatibility profile: integrated in vitro and in vivo characterization, Mater. Today Bio 38 (2026) 103225.